

Morphogenesis of digitate structures in hot spring silica sinters of the El Tatio geothermal field, Chile

Jian Gong^{1,2}  | Carolina Munoz-Saez³ | Dylan T. Wilmeth^{1,4}  | Kimberly D. Myers¹ | Martin Homann⁵ | Gernot Arp⁶  | John R. Skok⁷ | Mark A. van Zuilen¹ 

¹Université de Paris, Institut de Physique du Globe de Paris, CNRS, F-75005, Paris, France

²Department of Earth, Atmospheric and Planetary Sciences, Massachusetts Institute of Technology, Cambridge, Massachusetts, USA

³Nevada Bureau of Mines and Geology, University of Nevada, Reno, Nevada, USA

⁴Equipe Géomicrobiologie, Institut Universitaire Européen de la Mer, Plouzané, France

⁵Department of Earth Sciences, University College London, London, UK

⁶Geobiology Division, Geoscience Centre, Georg-August-Universität Göttingen, Göttingen, Germany

⁷SETI Institute, Mountain View, California, USA

Correspondence

Jian Gong, Department of Earth, Atmospheric and Planetary Sciences, Massachusetts Institute of Technology, Cambridge, Massachusetts, USA
 Email: gojian@mit.edu

Funding information

European Union's Horizon 2020 Research and Innovation Programme; Grant/Award Number: 646894

Abstract

In silica-rich hot spring environments, internally laminated, digitate sinter deposits are often interpreted as bio-mediated structures. The organic components of microbial communities (cell surfaces, sheaths and extracellular polymeric substances) can act as templates for silica precipitation, therefore influencing digitate sinter morphogenesis. In addition to biologic surface-templating effects, various microenvironmental factors (hydrodynamics, local pH and fluctuating wind patterns) can also influence silica precipitation, and therefore the morphology of resulting digitate sinters. Digitate sinter morphology thus depends on the dynamic interplay between microenvironmentally driven silica precipitation and microbial growth, but the relative contributions of both factors are a topic of continuing research. Here we present a detailed study of digitate silica sinters in distal, low-temperature regimes of the El Tatio geothermal field, Chile. This high-altitude geothermal field is extremely arid and windy, and has one of the highest silica precipitation rates found in the world. We find that digitate silica sinters at El Tatio always accrete into the prevailing eastward wind direction and exhibit laminar growth patterns coinciding with day-night cycles of wind- and thermally driven evaporation and rewetting. Subaerial parts of digitate sinters lack preserved organics and sinter textures that would indicate past microbial colonization, while filamentous cyanobacteria with resistant, silicified sheaths only inhabit subaqueous cavities that crosscut the primary laminations. We conclude that, although fragile biofilms of extremophile micro-organisms may have initially been present and templated silica precipitation at the tips of these digitate sinters, the saltation of sand grains and precipitation of silica by recurrent wind- and thermally driven environmental forcing at El Tatio are important, if not dominant factors shaping the morphology of these digitate structures. Our study sheds light on the relative contributions of biogenic and abiogenic factors in sinter formation in geothermal systems, with geological implications for the cautious interpretation of stromatolite-like features in ancient silica deposits on Earth and Mars.

This is an open access article under the terms of the Creative Commons Attribution-NonCommercial License, which permits use, distribution and reproduction in any medium, provided the original work is properly cited and is not used for commercial purposes.

© 2021 The Authors. *Geobiology* published by John Wiley & Sons Ltd.

1 | INTRODUCTION

Silica sinters are surface expressions of geothermal activity, produced when amorphous silica (opal-A) precipitates via cooling and evaporation from hot, silica-supersaturated groundwater discharged by hot springs (e.g. Fournier & Rowe, 1966; Hurwitz & Manga, 2017). In distal, low- to mid-temperature regimes (<50°C) of these geothermal outflows, microbial mats are ubiquitously present (Cady & Farmer, 1996; Jones et al., 1997; Lynne, 2012; Pepe-Ranney et al., 2012; Tobler et al., 2008; Walter et al., 1972). In many hot spring settings, particularly locations with alkali chloride fluids, these microbial mats are populated by cyanobacteria. The cell surfaces, resistant sheaths, and extracellular polymeric substances (EPS) of cyanobacteria act as templates for silica precipitation (Benning et al., 2004; Cady & Farmer, 1996; Handley et al., 2008; Jones et al., 2004; Jones & Renault, 1997; Konhauser et al., 2004; Renaut et al., 1996, 1998), generating sinters with various stromatolitic morphologies that are often interpreted as macroscopic biosignatures (Bosak et al., 2009, 2010, 2012; Cady & Farmer, 1996; Cady et al., 2003; Gong et al., 2020; Guido et al., 2019; Guidry & Chafetz, 2002, 2003; Jones & Renault, 1997; Pepe-Ranney et al., 2012; Petroff et al., 2010, 2013; Ruff & Farmer, 2016; Shepard & Sumner, 2010; Walter et al., 1972; Walter & Des Marais, 1993).

In high-temperature regimes (>50°C) directly surrounding geyser mounds or spring pool rims, stromatolites composed of thick silicified microbial mats are absent, but silica spicules, nodules and columnar sinters are found in which thinner biofilms of (hyper)thermophile micro-organisms occur (Cady & Farmer, 1996; Guido et al., 2019; Handley et al., 2005, 2008; Jones et al., 1997; Sriaporn et al., 2020). The fragile organic remains of micro-organisms in higher-temperature zones are relatively poorly preserved, making it often difficult to demonstrate a direct link between these biologic templating processes and resulting silica fabrics, laminations and morphologies. Yet, several studies, for example, conducted in geothermal fields of the Taupo Volcanic Zone at Rotorua (New Zealand), indicate that higher-temperature biofilms, similar to the lower-temperature, thicker distal microbial mats, display self-organization patterns, engage in recolonization of surfaces leading to upward growth, and are thus involved in the morphogenesis of these silica sinter structures (Handley et al., 2005, 2008; Sriaporn et al., 2020).

In addition to the general biologic surface-templating effect by microbial mats and biofilms, there are microenvironmental factors that affect the rate of silica precipitation and therefore the process of silica sinter morphogenesis, including local hydrodynamics, local pH, and fluctuations of wind and steam (Braunstein & Lowe, 2001; Handley et al., 2005, 2008; Schintie et al., 2007; Sriaporn et al., 2020). For instance, at Yellowstone National Park (USA) Braunstein and Lowe (2001) recognized a close relationship between local hydrodynamics of hot springs and geysers and the morphology of directly surrounding silica sinters. In the direct vicinity of such springs, the main drivers for sinter morphogenesis are the character of spring eruption, release of boiling or non-boiling fluids, and magnitude of water-level fluctuations (wave action, surging). Some of these

processes lead to repeated wetting and evaporation cycles, creating layered and branching sinter structures that resemble columnar or pseudocolumnar stromatolites (Braunstein & Lowe, 2001).

The overall morphology of silica sinter structures in geothermal fields is therefore the result of a dynamic relationship between the microenvironmentally driven rate of silica precipitation and the growth rate of microbial communities (Handley et al., 2005, 2008; Schintie et al., 2007; Sriaporn et al., 2020). When investigating these parameters in the field, one question that arises is whether there are specific geothermal settings where silica precipitation can outpace microbial growth, resulting in sinter morphogenesis dominated by microenvironmental factors alone. Careful study of sinter morphologies in such settings, and assessment of the underlying environmental factors that contributed to their formation, can help unravel the complex interplay between biologic and abiologic mechanisms of sinter growth. The study of sinter formation where microbial templating is minimal or absent is essential for understanding abiotic depositional processes and testing null hypotheses for biogenicity in deep time and astrobiology, such as purported ancient hot spring deposits on the surface of Mars (Ruff et al., 2011; Squyres et al., 2008) that contain intriguing silica sinter growth morphologies (Ruff et al., 2020; Ruff & Farmer, 2016).

Here we present a detailed study of digitate silica sinters—finger-like growth structures (Lowe & Braunstein, 2003; Lynne, 2012; Ruff & Farmer, 2016)—that form ubiquitously in distal, low-temperature regimes of the El Tatio geothermal field, Chile. This high-altitude geothermal field is extremely arid, windy and has one of the highest silica-precipitation rates found in the world (Munoz-Saez et al., 2020; Slagter et al., 2019). We describe the spatial distribution and orientation of these digitate sinters, their texture and composition in cross-section, and the distribution of microbial communities in both their subaerial and submerged components. These collective observations are then compared with the local microenvironmental conditions, including wind patterns, fluctuations in temperature and humidity, and water level changes. We show that the morphology of these digitate structures at El Tatio is predominantly determined by environmental forcing, while the growth of local microbial communities has a minor effect at best.

2 | GEOLOGICAL SETTING AND SAMPLE DESCRIPTION

El Tatio is situated in the Andes Mountains near the Chilean-Bolivian border, ca. 4300 m above sea level, associated with the Altiplano-Puna Volcanic Complex which is dominated by andesitic and rhyolitic ignimbrite deposits (Lucchi et al., 2009) (Figure 1a). The environmental conditions at El Tatio are extreme, with an average mid-day UV-B intensity above 6 W·m⁻², meteoric precipitation less than 100 mm·year⁻¹, an annual mean evaporation rate of 131.9 mm/day and air temperature shifting from 8–11°C during the day to -30–0°C at night (Cabrol et al., 2014; Fernandez-Turiel et al., 2005; Nicolau et al., 2014). The geothermal waters at El Tatio have a low boiling

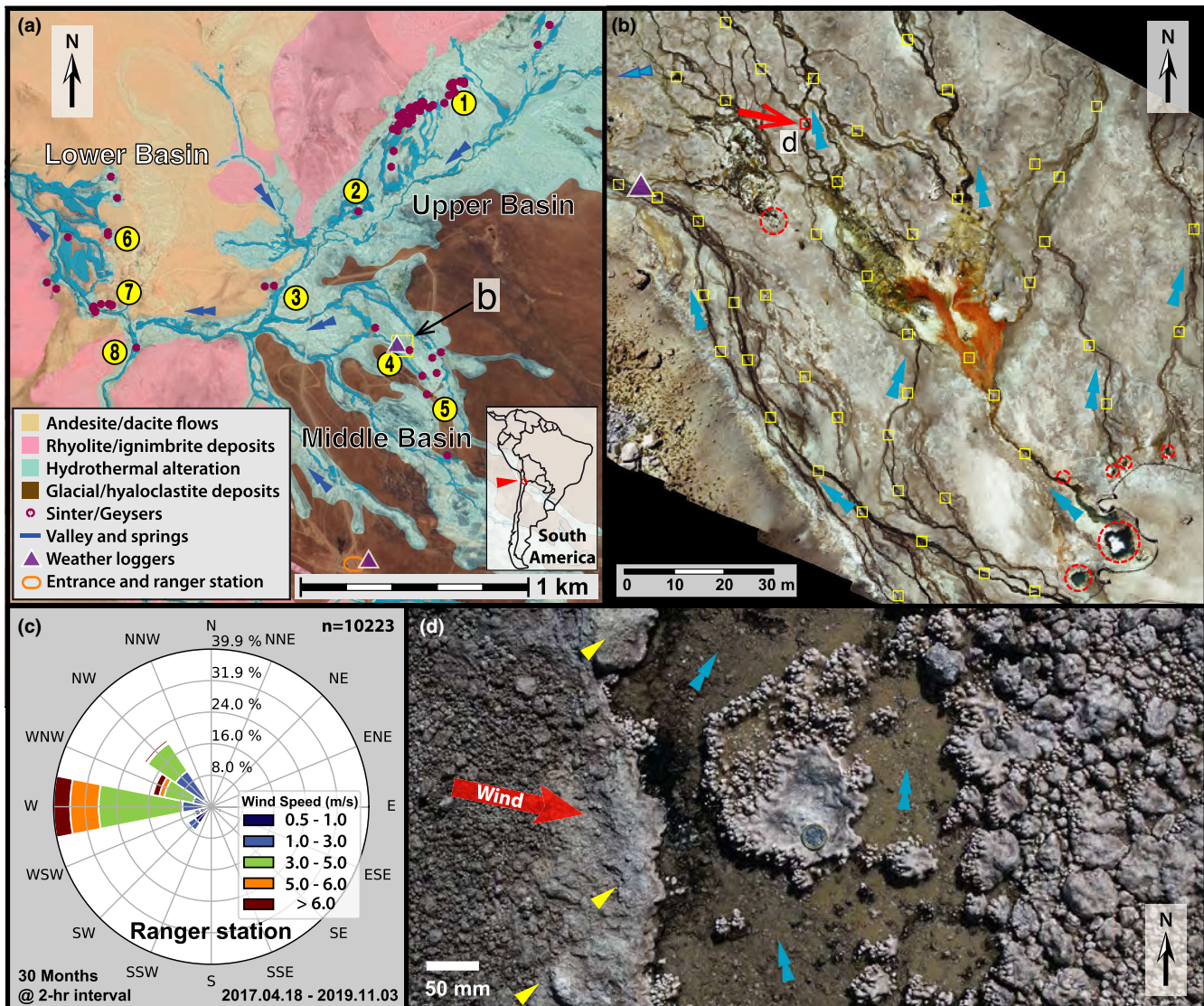


FIGURE 1 Spatial distribution and macro-morphology of digitate silica structures at El Tatio. (a) Regional geologic map of the El Tatio geothermal field, modified from Hurwitz & Manga, 2017. (b) Detailed aerial drone map of one study region at Middle Basin (blue arrows, channel flow directions; yellow squares, mapped digitate structures; red circles, spring outputs; red rectangle, the ground photo location in [d]). (c) Wind rose indicating wind direction (probability distribution in %) and speed (m/s). (d) Top-down view of a flow channel, where digitate structures occur predominately on a single bank of the channel (yellow arrows, absence of digitates on dry surfaces)

point ~86°C (Hurwitz & Manga, 2017) and are characterized by high levels of sodium and chloride ions ($[Na^+]$ up to 4650 ppm, $[Cl^-]$ up to 8100 ppm) and dissolved silica ($[SiO_2]$ up to 319 ppm) (Munoz-Saez et al., 2018), although in many springs, silica appears to be undersaturated (Cortecchi et al., 2005; Fernandez-Turiel et al., 2005; Munoz-Saez et al., 2018; Tassi et al., 2005). Due to high elevation and the specific dry, desert environment, the rate of water evaporation is the highest among geothermal springs around the world (Munoz-Saez et al., 2020; Slagter et al., 2019).

A total of 27 samples from eight locations within the three main basins of El Tatio were studied (Figure 1a, Table S1, Figure S1), including an area in the Middle Basin previously compared to a silica deposit in Gusev Crater (Ruff & Farmer, 2016) (Figure 1b).

3 | METHODS

3.1 | Field observations and measurements

Fieldwork was carried out at El Tatio, northern Chile during April, 2017, May 2018 and August, 2018. Field photos were taken with a Pentax K5 DSLR camera equipped with an external GPS sensor (Pentax O-GPS1), so that both GPS location and the orientation of the camera were recorded in every image. Long-term meteorological data including temperature, wind speed-orientation, relative humidity as well as atmospheric pressure were collected with a weather station that was installed on site near the entrance to the El Tatio Geothermal Field (GPS: 22°21'3.4" S, 68°0'54.3" W), which is about

1 km away from the main hydrothermal field (Vantage Vue; Davis Instruments). Weather data were collected from 18 April to 1 May 2017 at 10-min intervals and for an extended period at 2-h intervals until 27 April 2018. Short-term, complementary weather data including wind speed, orientation, air temperature, pressure and humidity were collected on site with a portable weather meter (Kestrel 5500; Kestrel Instruments) mounted on a tripod with the anemometer positioned at 37 cm above ground (GPS: 22°20'30.6" S, 68°0'49.9" W). Water temperature, ambient light level and surface temperature in selected locations were also recorded with data loggers (HOBO MX2202 and MX2203, Onset Computer Co. MX2202: temperature accuracy $\pm 0.5^\circ\text{C}$, range -20° to 70°C in air and -20° to 50°C in water; light level accuracy $\pm 10\%$ for direct sunlight, range 0 to 167,731 lux. MX2203: temperature accuracy $\pm 0.25^\circ\text{C}$ from -20° to 0°C and $\pm 0.2^\circ\text{C}$ from 0° to 70°C). Water temperatures were logged with the sensor fully submerged.

3.2 | Field drone mapping

An aerial drone map was acquired in April 2017 using a DJI Mavic Pro with the on-board camera at 12MP resolution. Images were recorded to ensure that most surface points would be captured by more than five overlapping images. The images were stitched together using the commercially available Pix4D Mapping Software to combine 1627 images, recorded from a height of ~ 33 meters, into a 0.21 km^2 map with a resolution of 1.03 cm/pixel. Higher-resolution drone images were additionally acquired in May 2018, with the drone flying at a lower height of ~ 20 m. These images in combination with field notes, photos and GPS waypoints, were used to construct a map of the digitate sinter structure locations (Figure 1b).

3.3 | Optical microscopy, SEM and EPMA

Field samples were collected in sterile plastic bags (VWR #BURK5344) or sterile plastic Falcon tubes, transported in dark and cold insulating bags, and stored in refrigerators immediately off the field at 4°C until analysis. Samples intended for mineral and compositional analysis were air dried in a sterile laminar flow hood for 3–7 days, embedded in epoxy (Buehler EpoxiCure 2) at room temperature, and cut and polished with pure mineral oil (Acros Organics 41508) to prevent dissolution of salts (following Ruff & Farmer, 2016). A second set of field samples, intended for imaging of biological components, was collected and stored in a different way. These samples were fixed on-site directly with 2.5% glutaraldehyde solution (prepared with filter-sterilized local spring water, following Cady & Farmer, 1996). Fixed samples were first rinsed twice in DI water (5 min each), and then dehydrated through an ethanol series (30%, 50%, 70%, 90% and 100% $\times 2$; 10 min each) (Handley et al., 2005, 2008). After dehydration, samples were critical-point dried using a Leica CPD 300, mounted on aluminium SEM stubs and sputter-coated with platinum using a Leica EM ACE600. All optical studies

of embedded, polished samples were performed at the Institut de Biologie Paris Seine (IBPS) using a Zeiss Axio Zoom.V16 motorized stereo microscope. SEM analysis was performed at the IPGP PARI analytical platform with a Zeiss GeminiSEM 500 at 3 kV and a working distance of 5 mm. EDX spectra and maps were obtained at 15 kV and 8.5 mm working distance on the same system. Electron Probe Microanalysis (EPMA) was performed at the UPMC analytical platform MEN (Microanalyses en sciences de l'Environnement) with a Cameca SX-Five system at 15 kV and 10 nA probe current configuration.

3.4 | Sample analysis by micro X-ray Fluorescence scanning

The spatial distribution of major and trace elements was detected and mapped on the dry cut surface of an unembedded digitate sample using micro X-ray fluorescence (μ -XRF). μ -XRF analysis was performed on a Bruker M4 Tornado instrument (Bruker Corporation) in the Geosciences Ocean facilities at the Institut Universitaire Européen de la Mer (IUEM), Plouzané, France. Mapping was done using 50 kV and 600 μA X-ray settings with no filter under 20 mbar vacuum. Elemental fluorescence data were obtained at a pixel size of 18 μm for an 8 ms dwell time, over a scanned area of $30.3 \times 51.1 \text{ mm}$ (1683 \times 2840 pixels). Final false-colour images were prepared using ImageJ by combining a chosen subset of elemental scans into a composite coloured image. Intensity and contrast of each colour were manually adjusted for optimal display. No other treatments were performed on the images.

3.5 | Laser Scanning Microscopy

Field sinter samples for Laser Scanning Microscopy (LSM) were chemically fixed on site following the exact protocol of Handley et al. (2008): Fixation for 3 h with fresh solutions of 4% paraform-aldehyde in pH 7.2 phosphate-buffered saline (PBS; 10 mM sodium phosphate buffer [Sambrook & Russel, 2001], 130 mM NaCl), followed by thorough 2x washing with PBS. Samples were then stored at 4°C in moist 50 ml Falcon tubes. After dehydration in a graded ethanol series (15-30-50-70-90-99-99%, each step 1 h) and en-bloc staining with Sytox Green (Thermo Fisher Scientific S7020; diluted 1:5000 in 50% EtOH/PBS), two samples were embedded with LR White (LR White resin, medium grade; London Resin Company Ltd.) according to the manufacturer's instructions, sectioned with a saw microtome SP 1600 (Leica) to a thickness of 500 μm , mounted on glass slides with Araldite 2020 epoxy resin (Huntsman Advanced Materials Europe), and ground down to a final thickness of 50 μm . One LR White section of each sample was additionally treated with 10% KOH and Calcofluor White staining solution (Fluka 18909-100 ml-F) for 10 min in the dark, washed with PBS and sealed with a cover slip. The fluorochrome Sytox Green was used for imaging of nucleic acids (Langsrud & Sundheim, 1996) while the fluorochrome

Calcofluor White was used for imaging of EPS (binding specifically to polysaccharides containing contiguous (1–4)- β -D-glucopyranosyl units; Wood, 1980). Sample sections were studied using a LSM 510 Meta NLO attached to a Axiovert 200 M microscope (Carl Zeiss Microlimaging, Jena) at the Geoscience Centre, Geobiology Group, University of Göttingen. Imaging was conducted at 40x and 63x magnification with water immersion. Excitation was achieved with Ar- and two HeNe-lasers at 488, 543 and 633 nm, while emission wavelength ranges were recorded at 500–530, 565–615 and 640–700 nm; Green channel (ex 488 nm/em 500–530 nm): unspecific autofluorescence, plus Sytox Green signal; Yellow channel (ex 543 nm/em 565–615 nm): unspecific autofluorescence; Red channel (ex 633 nm/em 640–700 nm): unspecific autofluorescence, including possible contents of photopigments such as chlorophyll. All three channels produced images because of amplification of even weak signals, and because all fluorochromes or pigments have some minor emission apart from their emission maximum. Emission fingerprinting and linear unmixing was carried out using a 32-channel diode array (Metadetector) and software of Carl Zeiss Microlimaging, Jena. Chalcofluor White signals were imaged using a femtosecond-pulsed Titan-Saphir-Laser Chameleon XR (Coherent, Dieburg), with 720 nm excitation wavelength and detection at 435–485 nm emission wavelength.

4 | RESULTS

4.1 | Environmental conditions at El Tatio

Meteorological data measured at the ranger station near the entrance of the El Tatio geyser field ($22^{\circ}21'3.4''$ S, $68^{\circ}0'54.3''$ W, ~1 km from the central geothermal region; Figure 1a and Figure S1) over a 30-month period (Figure 1c) indicate a consistent east and south-east wind direction. On-site measurements (Figure 1a) over the course of a 4-day period in the Middle Basin, confirm this wind direction (Figure S2a) and show that the wind follows a rhythmic diurnal cycle (Figure 2a). There is essentially no wind at night, but wind intensity rises about 2–3 h after sunrise every morning. At night, local air temperature drops to between -5 and -10°C , and reaches dew point, while the spring water temperature at a fixed location stays roughly constant at around 5°C (measured from 5 to 8 May 2018; Figure 2b). These local conditions would likely cause water vapour to condense onto relatively colder subaerial surfaces. Relative humidity shows an inverse relationship with wind intensity and air temperature (Figure 2b). In the mornings, relative humidity drops sharply from 90% to 30%–40% as wind speed increases, staying relatively constant during the day and slowly increasing during the night. During the day, water temperature rises to ca. $22\text{--}25^{\circ}\text{C}$ then falls, following in time the air temperature as well as the change in luminosity (Figure 2). The diurnal cycle of solar radiation and wind generation therefore appears to drive cyclic evaporative conditions. This rhythmic diurnal pattern of wind speed, air temperature and humidity was observed throughout 2.5 years of data collection at the

ranger station near the entrance (Figures S2–S4). Over longer time scales, intervals where anomalously high wind coincides with low atmospheric pressure conditions are interpreted as storm events. These events (e.g. Figure S2), together with seasonal variations in temperature, provide long-term sources of environmental variability in El Tatio.

4.2 | Distribution and orientation of digitate sinter structures

In all studied areas, we observed that digitate sinters are primarily subaerial morphologies that form at the edge of water bodies, including edges of shallow terrace pools and outflow channel banks (Figure 1d and Figure S5). In contrasts, digitate sinters are absent in dry, elevated areas away from any direct water source (yellow arrows in Figure 1d and Figure S6). Digitate structures appear to have a narrow height range at 5–22 mm above the water line (Figure S7 and Table S1), irrespective of water temperature (ranging from 3 to 64°C , Table S1) and distance from hydrothermal sources (ranging from areas directly adjacent to geyser splash zones, Figure S8a-d, to distal channels up to 268 m away, Table S1, Figures S5–S7). The ubiquitous occurrence of digitate structures at various distances from geyser activity distinguishes them from nodular (Figure S8e), spicular (Figure S8f), or columnar subaerial sinter structures that form by precipitation from splashed fluids within vent-proximal zones (Braunstein & Lowe, 2001; Handley et al., 2005; Jones & Renaut, 1997, 2003; Lowe & Braunstein, 2003; Lynne, 2012; Mountain et al., 2003). At all studied locations in the three El Tatio basins, digitate structures have a characteristic uniform orientation, consistently tilting toward the west/northwest direction (tilt angle varying from 37° to 75° , Table S1), regardless of the position of the water sources and thermal fluid flow directions (Figure 1, Figures S5–S8).

4.3 | Internal structure of the digitate sinters

Individual digitate structures in cross section show a laminated growth pattern of alternating white and brown layers (Figure 3; air-dried sample, epoxy-embedded side). Laminae are convex-upward, specifically thickened at the windward side, leading to tilted growth directions up to 75° from surface normal (Figure 3d,e; Table S1). This distinctive tilt is not correlated with local fluid flow directions (Figure 1d, Figures S5 and S6), but with preferential accumulation of granular material at the windward side of the digitate structure (Figure 3e: blue arrows), as well as in topographical lows behind the digitate structure (Figure 3e: green and red arrows). These observations provide strong evidence for subaerial, lateral deposition of sand grains on moist surfaces by wind-lift, saltation, and obstacle-generated vortices (Davies et al., 2016; Kocurek & Fielder, 1982; Kok et al., 2012; Olsen et al., 1989; Rice et al., 1995). The stacking of layers appears to be continuous below and above the water line. The subaqueous layers also contain sand grains, and in several

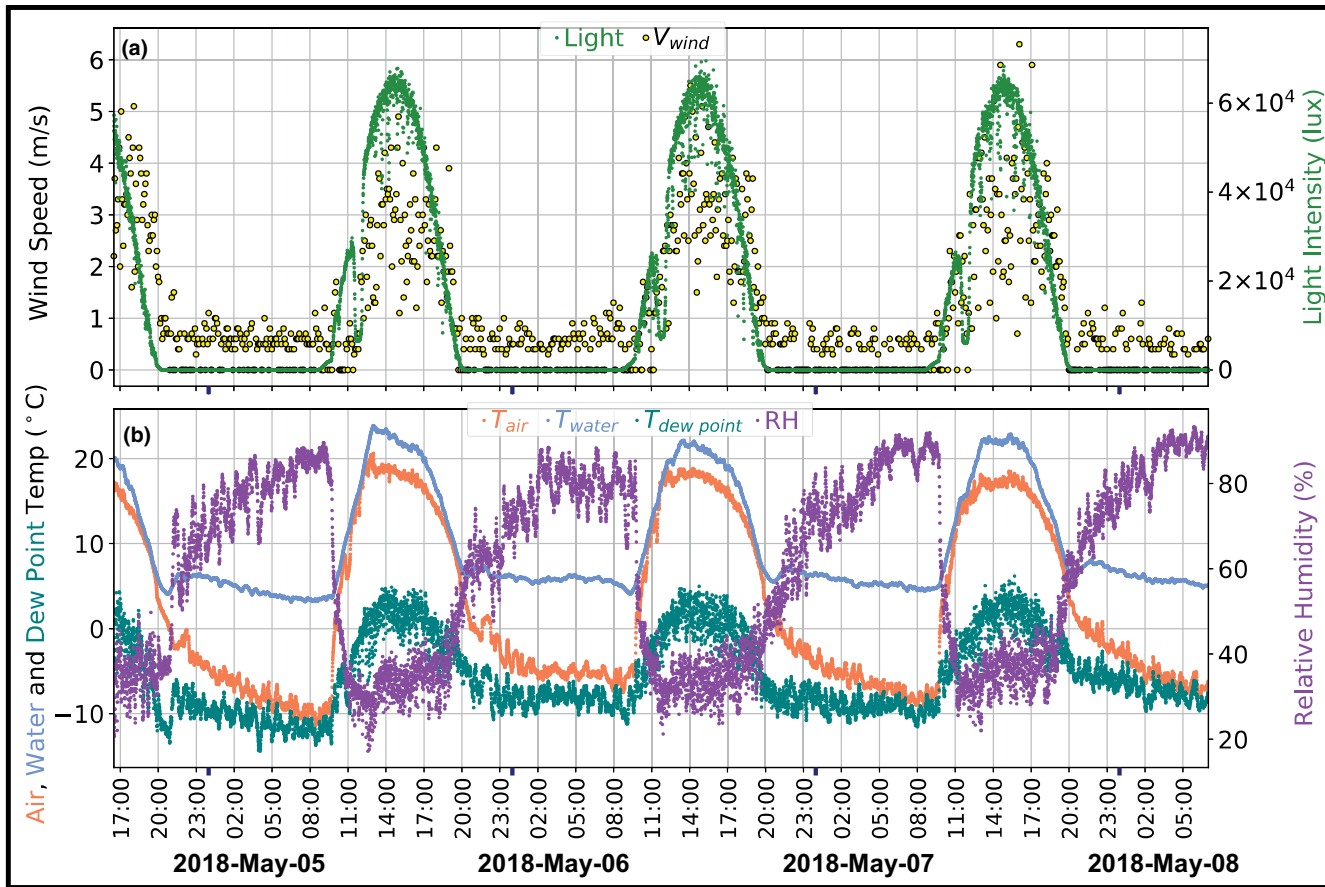


FIGURE 2 Plots of environmental data including air and water temperature ($^{\circ}$ C), air relative humidity (%), dew point ($^{\circ}$ C), wind speed (m/s) and light intensity (lux) from on-site data loggers placed directly next to a digitate structure formation at Middle Basin (location indicated in Figure 1 and Figure S1). All data were collected at 5-min intervals from 5 to 8 May 2018. (a) Combined wind speed and light intensity plot. Note that the dip of light intensity around 12:00 pm each day was due to a shadow caused on the light intensity sensor by the adjacent probe for air temperature/relative humidity. (b) Combined plot of air temperature, air relative humidity (RH), dew point and spring water temperature

cases show thickening and tilted growth in the same direction as the overlying subaerial layers (Figures 3c, 5a, 6a). Analysis of representative laminae by optical microscopy and SEM reveal that packages of laminae 200–300 μ m in thickness (Figure 3f) are composed of much finer, 2–20 μ m layers (Figure 3g: arrows, Figure S11a). These laminae curve around (Figure 3f) sand grains of different sizes, shapes and varying compositions with respect to Al, K and Si concentrations (Figure 3g,h and Figure S11a). Porosity within the laminae is primarily correlated with high concentrations of sand grains (Figure 3h and Figure S11a). EPMA analysis of sand grains confirms the presence of K-feldspar and plagioclase (Table S2), suggesting emplacement by transport from surrounding andesitic and rhyolitic ignimbrite deposits (Lucchi et al., 2009) (Figure 1a). Variations in the thickness of sand grain layers are common, with isolated layers containing higher abundances of larger grains than typically observed (Figure 3d-h and Figure S11a). These uneven intervals could possibly be linked to stochastic storm events (Figure S2c,d), and general long-term fluctuations in the local weather conditions (Figures S3 and S4).

Micro-XRF analysis (Figure S9a; air-dried sample, not embedded in epoxy), shows the distribution of Na and Cl (interpreted as NaCl,

halite) relative to Al (interpreted as detrital mineral grains) and Si (silica) (Figure S9b,c). El Tatio hot spring waters are characterized by high levels of sodium and chloride ions. As silica polymerization is further enhanced under high salt concentrations (Belton et al., 2012; Chan, 1989; Iler, 1979), thermal- and wind-driven evaporation of such fluids favour evaporative precipitation of both silica and salt, leading to effective cementation of sand grains. The high porosity of the digitate structures and the small amount of salt relative to silica (Figure S9b,c) suggests that salt is partially dissolved during rewetting.

4.4 | Micro-organisms in digitate sinters: Optical microscopy and SEM analysis

Microscopic examination of air-dried digitate sinters (Figure 3a) reveals the presence of sheathed filamentous cyanobacteria, visible as dark green coatings lining the bottom exterior surfaces (Figures 3b,c and 4, Figure S10). Cyanobacterial morphologies are defined by short-tapered filaments, terminal heterocysts, and frequent

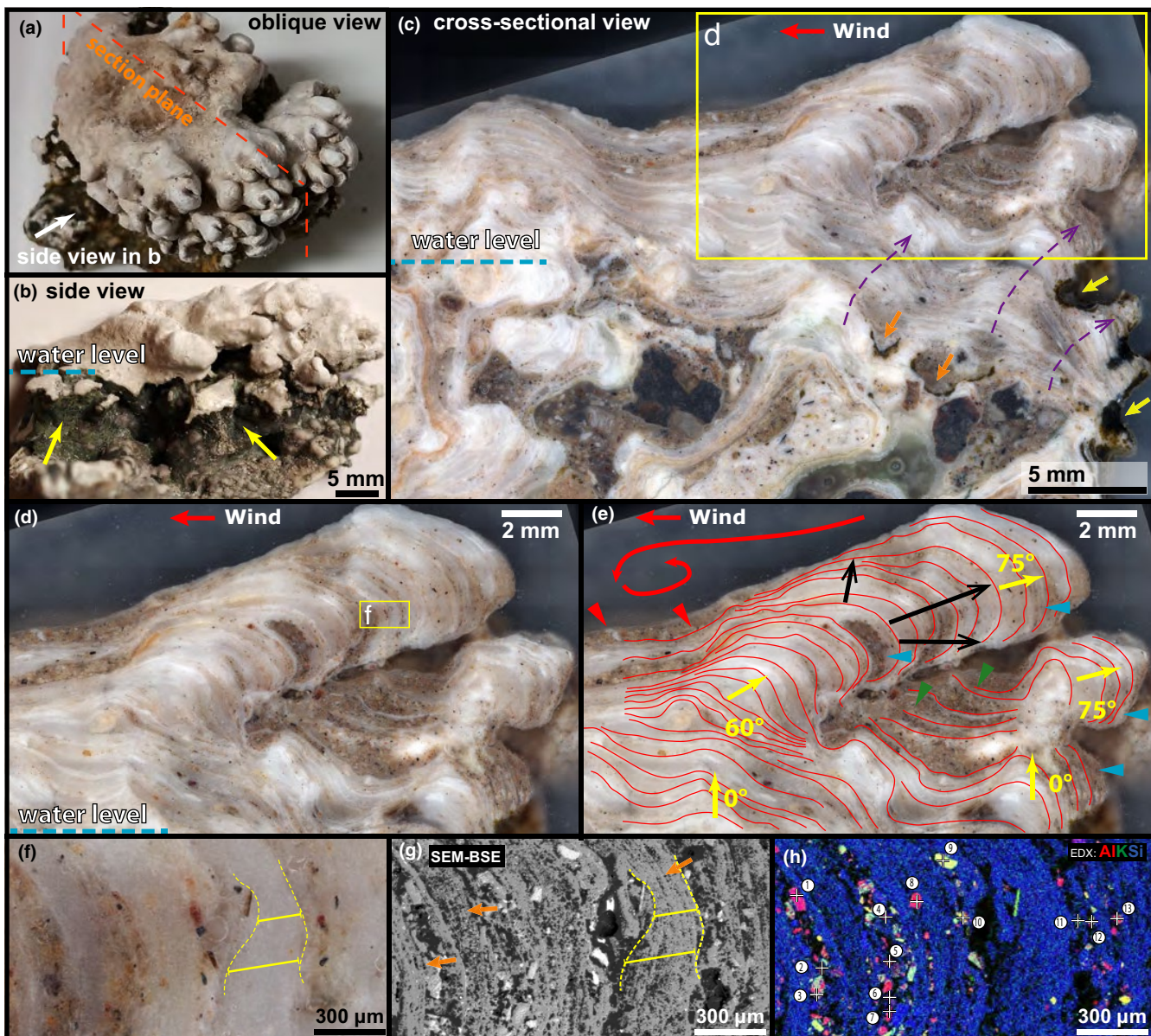


FIGURE 3 Cross section of a digitate structure from Middle Basin (Figure 1). (a) Oblique view of the sample with the cross-sectional cut position marked (also see this structure in 3 dimensions in Figure S10). (b) Side view showing dark microbial communities lining subaqueous surfaces (arrows). (c) Cross-sectional view of the digitate structure (yellow arrows, recent cavities; orange arrows, early cavities). (d) Close-up view of the subaerial structure, showing laminated growth morphology tilting into the wind. (e) Same image as in (d) with selected laminae manually traced (black arrows indicate different directions of accumulation rate causing non-isopachous lamination; yellow arrows indicate change in general growth direction from vertical to 60–75°; blue arrows, sand accumulation at the windward side; red arrows, sand accumulation in topographical lows). (f) Zoom-in of laminae and accumulated sand grains. (g) SEM Back-scattered electron (BSE) image of the same region in (f) (dashed lines: lamina curving around regions of sand deposition; orange arrows: fine laminations 2–20 µm thick). (h) SEM-EDX elemental map of region in (g), revealing the common presence of Al-rich, feldspar grains along the laminations. Numbered locations indicate analysis of selected grains from Electron Microprobe point measurements, with exact mineralogy reported in Table S2

false branching (Figure 4g,h), prompting assignment to the genus *Rivularia*, which can tolerate the salinities present in El Tatio waters (Castenholz et al., 2001; Mlewski et al., 2018). These biofilms were found to associate with degraded primary, laminated silica fabric (Figure 3b,c: yellow arrows, enlarged views shown in Figure 4a-e and Figure S11b), while well-preserved marks of earlier degradations are also observed (Figure 3c: orange arrows; Figure 4g,h). Degraded

zones also preserve palisade fabrics (Figure 4e,f), which are closely packed, regularly spaced, micro-pillar structures oriented surface-normal along the principal fabric direction (Gong et al., 2020; Guido et al., 2019; Lynne, 2012). Such palisade fabrics are often found in hot spring silica sinters, and are formed when populations of filamentous micro-organisms act as templates for silica polymerization (Belton et al., 2012). Visible evidence of microbial colonization,

such as remnant cellular structures, decreases drastically across the subaqueous–subaerial boundary (Figures 3c,d, 4–6), and is absent at the tops of all 27 digitate structure samples we examined microscopically (Table S1).

To ensure that microbial distribution within sinters is not an artefact of sample preparation, we preserved additional digitate samples (Figure 5a) using a direct field-based biological fixation protocol (see Methods). As with air-dried samples (necessary to prevent dissolution of salt), the subaerial zones of fixed digitate structures do not contain visible traces of remnant microbial structures or void spaces following the degradation of cellular material (Figures 5b,d–f,6c,d,h–m,7(zones A,B) and Figure S11A,C), whereas subaqueous zones contain biofilms associated with degraded

primary silica surfaces (Figures 5c,g–i,6a,b,e–g,7(zones C,D) and Figure S11B,D). High-resolution SEM images of the digitate sinter in Figure 5, show subaerial zones of silica sinter consisting of porous networks of large silica spheres (2 micron in diameter; zones A and B in Figure 7). However, we could not identify silicified cells or EPS in these subaerial regions. In the subaqueous part, recently colonized cavities show individual filamentous cells and EPS covered by very small silica spheres (ca. 100 nm diameter; zone C in Figure 7). An older cavity zone shows more strongly silicified filamentous micro-organisms, and silica spheres are ca. 1–2 micron in diameter (zone D in Figure 7). This microbial colonization at and below water level suggests that the dominantly visible microbial communities inhabiting these structures preferentially colonize already existing

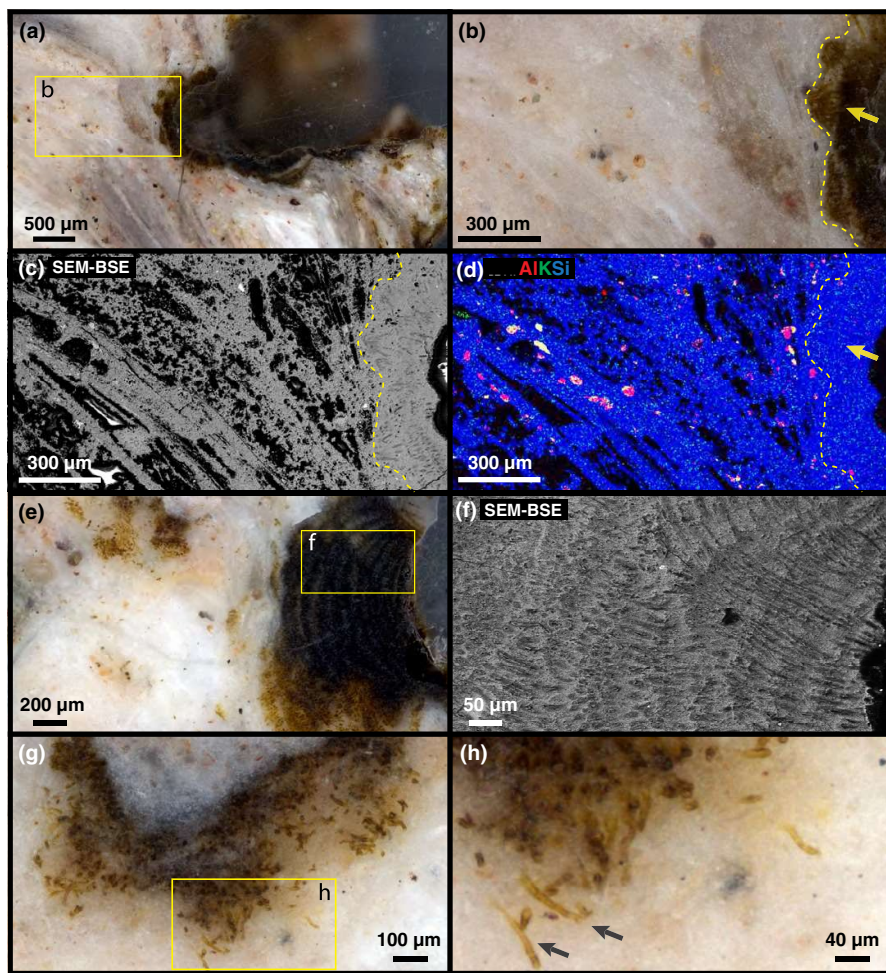
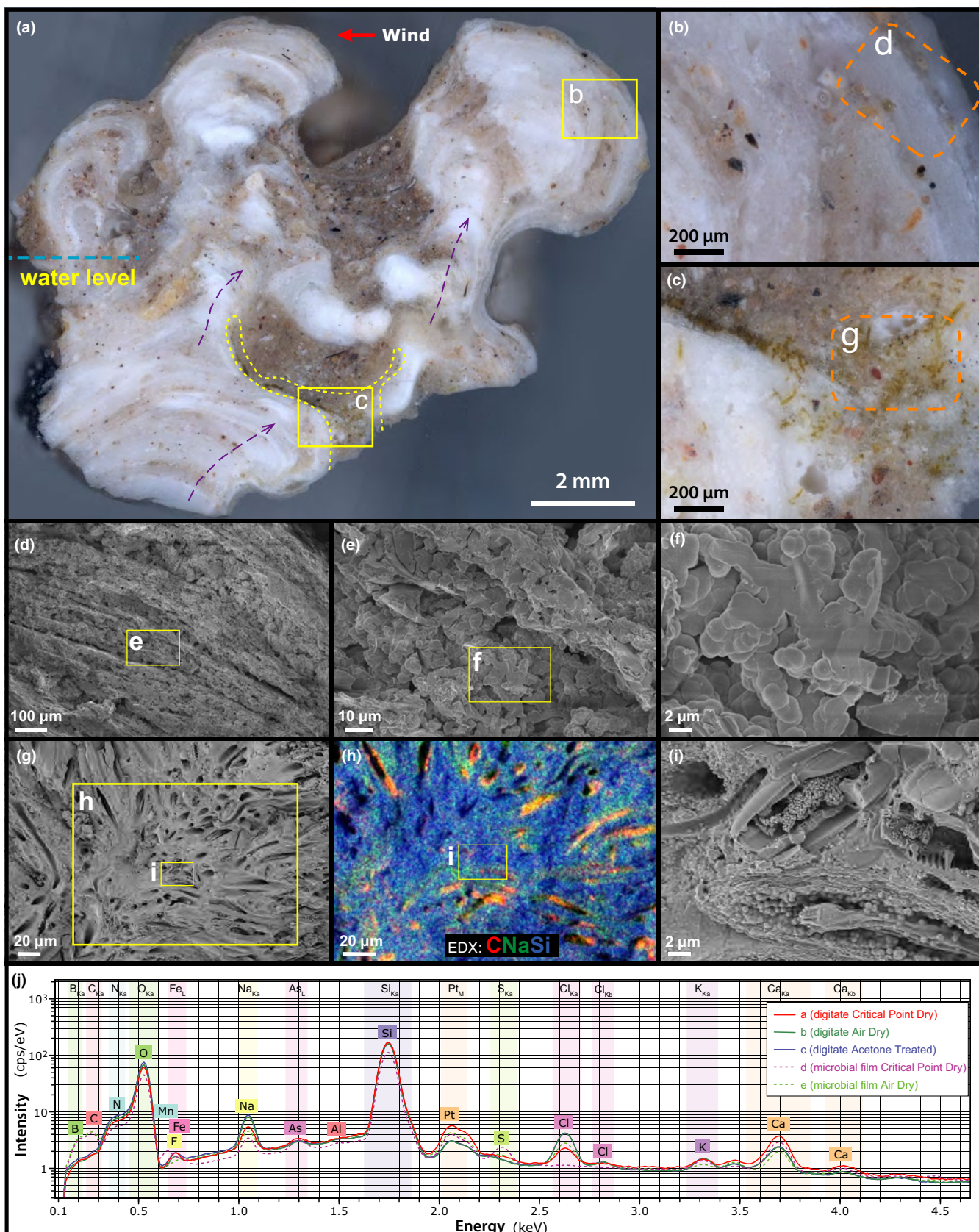


FIGURE 4 Preserved microbial fabrics. (a) Subaqueous cavity (image enlarged from Figure 3c) lined by dark green microbial community. (b) Enlarged view from (a), showing the microbial layer (arrow). (c) SEM-BSE scan of (b), showing detailed sinter fabrics. (d) EDX Al-K-Si false-colour elemental map of (b), showing previously deposited grains as well as the microbial layer free of grains (arrow). (e) Another subaqueous cavity (image also enlarged from Figure 3c), showing dark layers of consecutive microbial growth. (f) SEM-BSE scan of a selected region in (e), showing more clearly the characteristic palisade fabric made by filamentous bacteria. (g) View of a well-preserved formal cavity (image enlarged from Figure 3c). (h) Enlarged view from (g), showing the presence of individual sheathed filamentous bacteria

FIGURE 5 Digitate structure that was chemically fixed on-site. (a) Overview of the cross-sectional cut region. (b) Subaerial region showing the absence of any microbial traces. (c) Subaqueous region, showing the presence of filamentous bacteria. (d–f) SEM images of unembedded and critical-point dried subaerial digitate structure, corresponding to the boxed region in (b). (g) SEM image of unembedded and critical-point dried subaqueous digitate structure, corresponding to the boxed region in (c). (h) SEM-EDX map of the region in (g), showing the presence of organic carbon within sheaths. (i) Enlarged SEM image from the region in (h), showing silicified sheathed filamentous bacteria as well as diatoms living in a closely associated community. (j) SEM-EDX spectra of regions in chemically fixed digitate structure samples, showing remnant carbon only in the subaqueous parts where filamentous bacteria are found. The subaerial parts of the sinters do not show any trace of carbon. Four spectra of this sample are displayed: Subaerial digitate sample (corresponding to image in panel e); (a) critical-point dried and (b) room air dried. Subaqueous silicified microbial mats (corresponding to image in panel h) from the same sample: (c) critical-point dried and (d) room air-dried



submerged sinter zones, possibly degrading the surfaces to form cavities. Our observations here are in line with previous observations that microbial mats and biofilms are best developed in permanently wetted parts of hot springs, and are absent in exposed

areas (Lowe & Braunstein, 2003) where microbial growth is hindered through combined drying, high salinity, high UV radiation and rapid coating by precipitating silica (Harrison et al., 2013; Lowe & Braunstein, 2003).

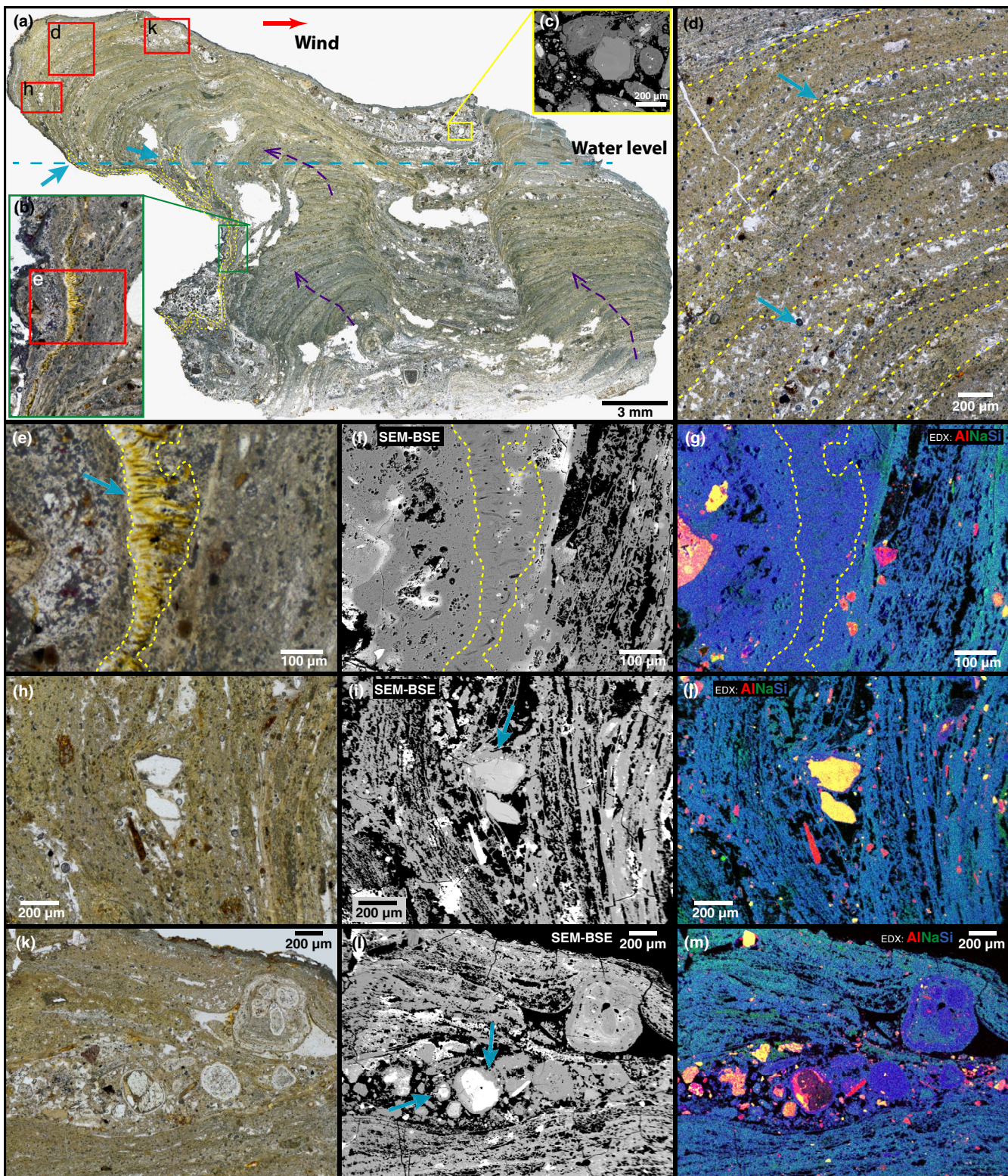


FIGURE 6 Microscope images of a thin-sectioned digitate structure, Middle Basin. (a) Overview of the sample cross section. The yellow dashed region indicates recognized presence of micro-organisms, which do not occur beyond a certain area (blue arrows). (b) Enlarged subaqueous region showing the presence of sheathed filamentous bacteria. (c) SEM-BSE image of a sand grain coated with silica. (d) Enlarged subaerial laminae region showing sensitivity of lamina morphology to the incorporated detrital grains (blue arrows). (e) Enlarged region from (b) showing silicified sheathed filamentous bacteria (blue arrow). (f) SEM-BSE scan from the same region in (e). (g) Element map of the same region in (e) and (f), showing absence of grains within the filamentous microbial cells. (h) Enlarged subaerial region from (a) containing some grains wedged in between laminae. (i) SEM-BSE scan of the same region in (h), showing silica coated grains (blue arrow). (j) Element map of the same region in (h) and (i). (k) Another enlarged subaerial region from (a) containing a few large grains. (l) SEM-BSE scan from the same region in (k), showing coated grains (blue arrows). (m) Element map of the same region in (k) and (l).

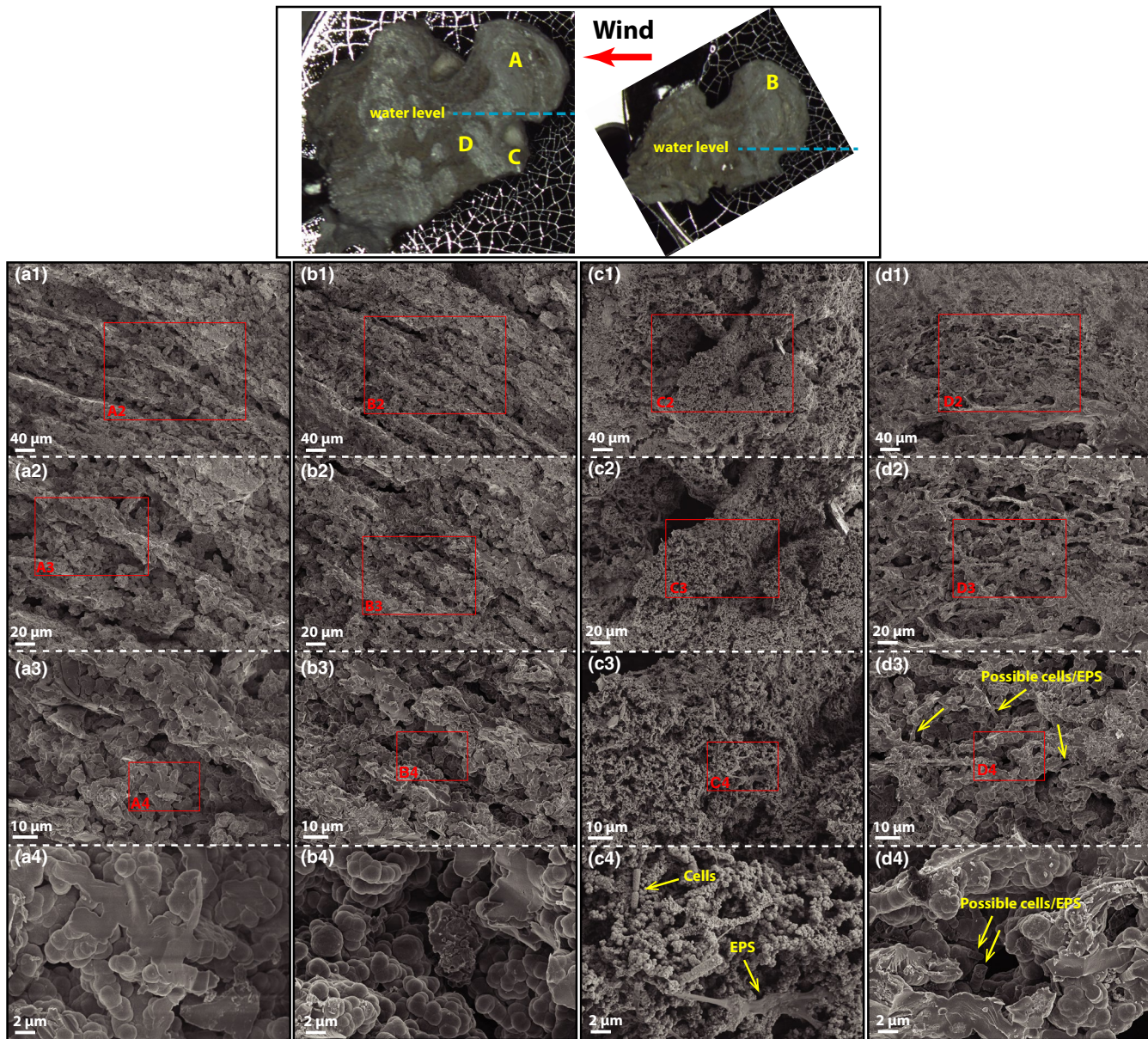


FIGURE 7 Detailed SEM images of subaerial digitate sinter structures. Top row: key locations of SEM images of two samples that have been chemically fixed and critical-point dried. (a1-a4): subaerial digitate sample, corresponding to images in Figure 5d-f. (b1-b4): a separate (duplicate) subaerial digitate sample, imaged using identical settings. Note the consistent lamina thickness, around 20 µm per layer across both samples and the uniform size of amorphous silica spheres at 1–2 µm diameter. No features or moulds of biofilm or cells were identified in these images. Discontinuous stacks or sheets of amorphous silica (opal) spheres are present, with extensive internal porosity. (c1-c4): subaqueous portion of the digitate sinter, imaged using identical settings, where abundant microbial cells and EPS can be identified. Note the much smaller size and non-uniform silica spheres at the cell/EPS surfaces, at 100 nm diameter or smaller. (d1-d4): subaqueous partition, interior of the digitate sinter sample, imaged using identified settings, where possible cells/EPS can also be identified

4.5 | Micro-organisms and EPS in digitate sinters: LSM analysis

Microbial cells and associated EPS can easily be missed by optical microscopy and SEM (Handley et al., 2005, 2008). For this reason, a detailed LSM study was performed on a specifically prepared sample, using a fluorophore—Calcofluor White—that binds to EPS (see Methods, Section 3.5). In order to observe EPS in relation to

microbial cells, another fluorophore—Sytox Green, binding to nucleic acids—was added. The digitate sinter sample was specifically studied for subaqueous (areas SG-1, SG-2 and SG-3) and subaerial (areas SG-4 and SG-5) parts along the surface of the digitate (Figure 8a). If microbial communities are creating surfaces that template silica precipitation, they should be found along the surfaces of the digitate sinters. In area SG-1, as is visualized with Sytox Green, large, sheathed filamentous bacteria are present (in line with the cyanobacterium

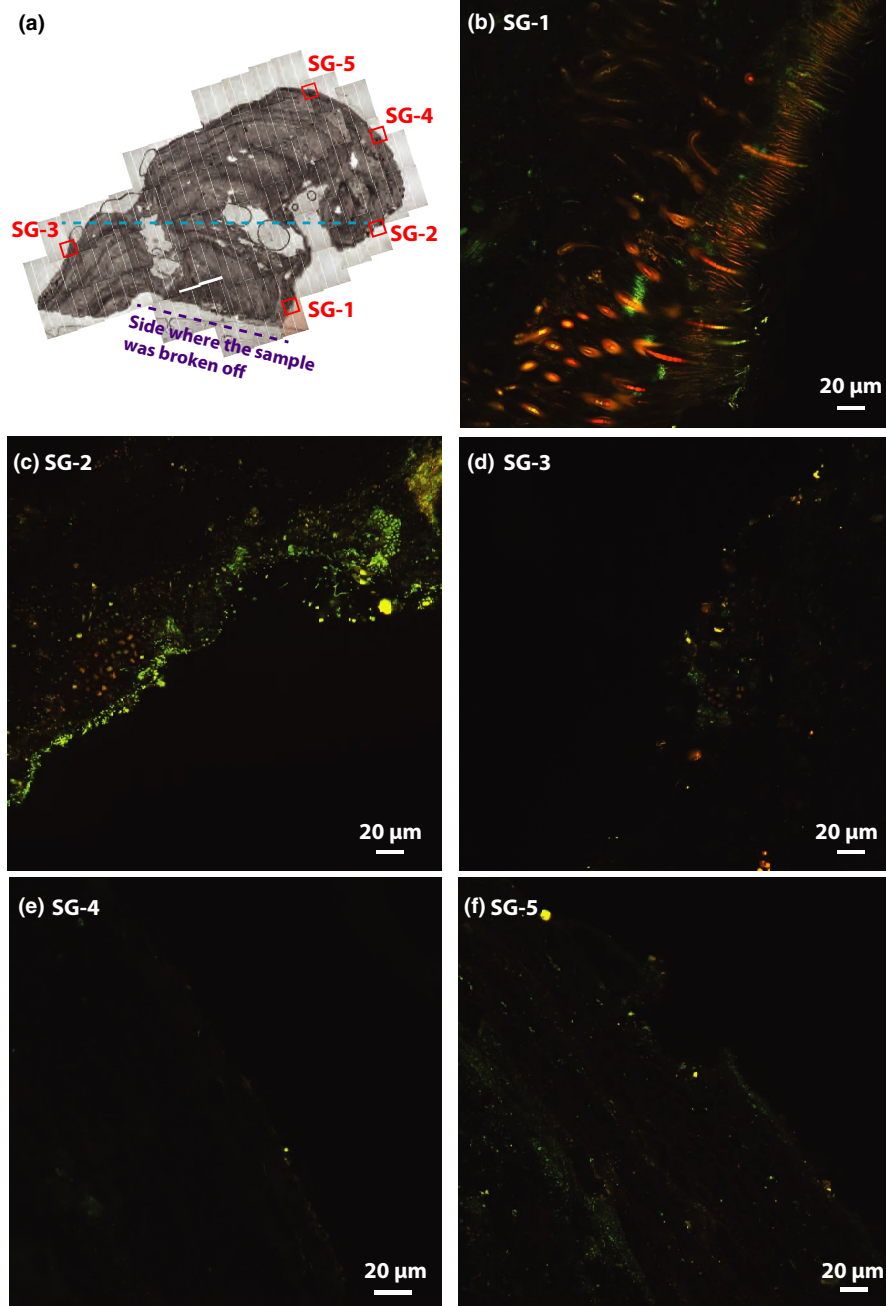


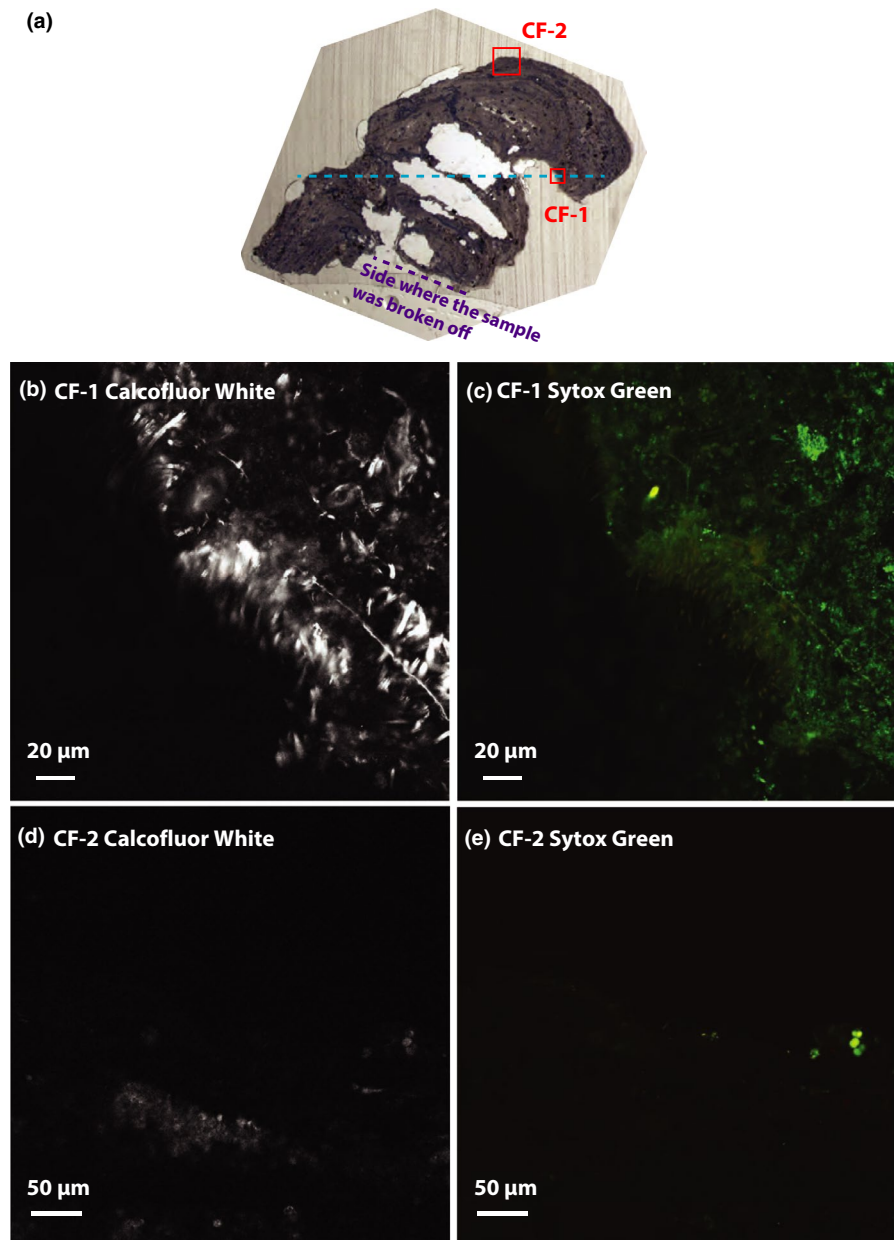
FIGURE 8 Laser scanning microscopy images of Sytox Green-stained digitate sinter sample (ex 488 nm, 543 nm, 633 nm/em 500–530 nm, 565–615 nm, 640–704 nm; all images recorded using the same scan parameters). (a) Sites for imaging of Sytox Green-stained sample. Subaqueous parts of the digitate sample are area SG-1, SG-2 and SG-3, subaerial parts are areas SG-4 and SG-5. (b) SG-1, showing large sheathed filamentous cyanobacteria identified as *Rivularia*, as well as an unidentified type of small filamentous bacteria. (c) SG-2, showing small filamentous bacteria (green), coccoidal micro-organisms (orange) and diatoms (yellow), (d) SG-3, showing coccoidal micro-organisms (orange), (e) SG-4, showing only a few stained sand grains and cracks, (f) SG-5, showing only a few stained sand grains and cracks

Rivularia sp.) as well as much smaller, unsheathed filamentous bacteria of unknown origin (Figure 8b, Figures S12, S13a,b). The large filaments are restricted to area SG-1, but the small filaments occur all along the digitate sinter surface towards area SG-2 (Figure 8c, Figure S13c). The entire zone from area SG-1 to area SG-2 clearly shows colonization of a cavity in the sinter structure. On the other subaqueous side of the digitate sinter, in area SG-3, coccoidal micro-organisms occur (Figure 8d, Figure S13d). The entire subaerial zone between area SG-2 and area SG-3—along the top of the digitate structure, including area SG-4 (Figure 8e, Figure S13e) and area SG-5 (Figure 8f, Figure S13f)—is devoid of any cellular structures.

The LSM images of the same digitate sample stained with Calcofluor White (Figure 9a) additionally show the presence of EPS in the subaqueous area CF-1 (Figure 9b and Figure S14a). It is

important to note that Calcofluor White was applied to the cutting surface of the section, whereas Sytox Green staining was applied to the bulk sample *en bloc* prior to sample embedding and sectioning. Therefore, the optical image plane of the Calcofluor White-stained section surface differs in few μm z distance from that of the Sytox Green-stained image. Despite this difference in optical plane, it is clear that EPS follows the morphology of the small filaments (as seen by Sytox Green fluorophore, Figure 9c and Figure S14b), and represents the polysaccharides of the sheaths surrounding the cyanobacterial trichomes. In contrast, area-CF-2 in the subaerial part (Figure 9d,e and Figure S14c,d) does not show presence of EPS. Some of the bright Calcofluor White staining within the mineralized material rather reflects unspecific binding to hydrous silica, detritus or cracks, but not necessarily polysaccharides. These LSM

FIGURE 9 Laser scanning microscopy images of Calcofluor White- and Sytox Green-stained digitate sinter sample. (a) Sites for imaging Calcofluor White- and Sytox Green-stained sample. Area CF-1 is subaqueous, area CF-2 is subaerial. (b) Area CF-1, Calcofluor White stain showing EPS of *Rivularia* sheaths (720 nm 2-photon-excitation, em 435–485 nm), (c) Area CF-1, Sytox Green-stain showing filamentous trichomes (ex 488 nm, 543 nm, 633 nm/em 500–530 nm, 565–615 nm, 640–704 nm), (d) Area CF-2, Calcofluor White stain showing no trace of any EPS (720 nm 2-photon-excitation, em 435–485 nm), (e) Area CF-2, Sytox Green-stain, showing only a few stained sand grains (ex 488 nm, 543 nm, 633 nm/em 500–530 nm, 565–615 nm, 640–704 nm)



observations complement the observations made by optical microscopy and SEM (see Section 4.4), suggesting that microbial activity is primarily observed in cavities in the subaqueous part of the digitate structure.

5 | DISCUSSION

The El Tatio geothermal field is a unique environment in which the relative contributions of biologic and abiologic factors in digitate sinter growth can be tested. Extremely dry conditions, large diurnal temperature fluctuations, and strong winds lead to large fluctuations in silica precipitation rates, and also provide challenging conditions for microbial community growth. The roles of microenvironmental and biologic effects are discussed in the paragraphs below.

5.1 | The role of microenvironmental factors in digitate sinter growth

Several observations at El Tatio indicate a strong influence of local physical conditions on the precipitation of silica and overall morphogenesis of the digitate sinters. The universal west/northwest orientation of digitate structures (Figure 1d and Figures S5–S8), directly into the prevailing east/southeast wind direction (Figure 1c and Figure S2a,b), combined with the diurnal fluctuation of wind speed and humidity (Figure 2 and Figures S2–S4) indicate that both thermal- and wind-driven silica precipitation and evaporation, as well as wind-driven sand deposition, are the likely dominant factors for tilted subaerial laminar growth. In contrast, despite the variable water flow directions at the local studied sites (Figure 1), the growth orientation of the digitate sinters appears to be consistently

unidirectional across the entire spatial scale of the geothermal field (Figure 1d and Figures S5–S8).

In cross-sections, all examined digitate structures appear to contain laminae with sand grains that predominantly accumulated at the windward side, causing the tilted growth pattern (Figures 3, 5, 6, Figures S9–S11). Sand grains in the sinters are occasionally associated with halite (Figures S9c, S17), suggesting evaporation during/after aeolian deposition. The stacking pattern of the digitate sinter laminae is continuous across the water line, and asymmetric, windward tilted morphologies are frequently observed in currently subaqueous portions of digitate sinters (Figures 3c, 5a, 6a). We interpret these textures as evidence for an initial subaerial wind-driven growth process, followed by a later increase in water level—possibly driven by seasonal or longer-term changes – leading to partial submergence of the digitate sinters.

One alternative scenario is that silica deposition occurred subaqueously and that the resulting digitate sinters were exposed subaerally at a later stage. The observed accumulation of sand at the west/northwest side of the sinters could occur if the uppermost water layers during sinter deposition were more strongly affected by the prevailing east/southeast wind than by local stream flow. Also, it could be argued that the observed salt (Figures S9c, S17) only formed in later stages when the digitate sinters were finally exposed.

Two key observations argue against a subaqueous sinter growth scenario. First, spring waters at El Tatio are typically silica-undersaturated despite relatively high concentrations at initial discharges (~150–270 ppm SiO₂, 75–90°C) (Cortecchi et al., 2005; Jones & Renault, 1997; Nicolau et al., 2014; Phoenix et al., 2006; Wilmeth et al., in press, 2021). Recent studies show that decreasing SiO₂ concentrations in downstream waters maintain undersaturated conditions in daylight hours (30–85°C), but night-time cooling (~30–+25°C) can saturate solutions and potentially foster subaqueous silica precipitation (Nicolau et al., 2014; Wilmeth et al., in press, 2021). However, night-time cooling still does not explain the observed uniform tilt in digitate sinters to the west/northwest, since wind is minimal at night (Figure 2). Any tilt in subaqueous sinter growth at night would be governed by local water flow directions, which is not supported by our observations. The consistently wind-oriented morphology of digitate sinters therefore argues against subaqueous silica precipitation. Second, digitate sinters are consistently found along the wind-facing banks of flow channels throughout the basin (Figure 1d, Figures S5–S8), while they are absent in the channels themselves. Such specific spatial distributions argue against subaqueous precipitation as a primary factor in sinter growth, which would hypothetically produce digitate structures throughout submerged streambeds.

5.2 | The role of biology in digitate sinter growth

Previous experiments have shown that subaerial exposure leads to higher rates of sinter encrustation and better preservation of cellular fabrics (Mountain et al., 2003) and that cyanobacterial sheaths are particularly resistant structures against post-depositional degradation (Bartley, 1996; Gong et al., 2020; Guido et al., 2019). Therefore,

if sheathed cyanobacteria had lived and died on the top of the digitate structure during subaerial exposure, then cells and sheaths would likely be encrusted in silica and preserved. Ruff and Farmer (2016) presented a detailed study of digitate sinters at El Tatio, and indeed reported silica encrusted cells, extracellular sheaths and EPS. However, this study noted that the filamentous cells/sheaths appear in relatively large fenestral cavities in between the finely laminated layers that themselves lack identifiable microfossils.

Our observations using optical microscopy, SEM and LSM, also confirmed the presence of communities of large, sheathed cyanobacteria, but only in sub-aqueous zones of digitate sinters. These microbial communities, appear to have secondarily colonized surfaces and cavities in pre-existing fabrics (Figures 3–6). Patterns of secondary colonization are observed in both living (Figures 3c, 4, 5c,g–i, 6a,b,e–g, Figure S11b,d) and silica-entombed cyanobacterial communities (Figure 3c Orange arrows, Figure 4g–h, Figure 7c,d). In contrast, exposed subaerial digitate surfaces in our samples did not reveal remnant cells, sheaths, moulds or fabrics (Figure 7a,b). This shows that communities of large, resistant micro-organisms such as cyanobacteria, although occasionally present, did not contribute to the laminar growth of the digitate sinters. Furthermore, the westward tilting of digitate structures does not support a photosynthetic/phototactic model of growth (Bosak et al., 2012, 2013; Petroff et al., 2010; Walter, 1976), as the averaged solar radiation at El Tatio comes from geographic north (Figure S15). If photosynthetic biofilms or microbial mats were responsible for the angled geometry of digitate structures, their integrated effects on sinter growth, whether constructional or erosional, should align close to the north–south axis of maximum sunlight. In light of our current observations we interpret the biomediated lamina in large fenestral cavities observed by Ruff and Farmer (2016), as secondary colonization features in an already existing finely laminated digitate sinter.

While sheathed cyanobacteria appear not to be responsible for the primary finely laminated digitate fabrics, the potential for more fragile, unsheathed micro-organisms to have acted as templates for silica precipitation remains a possibility. In other geothermal fields, biofilms of hyperthermophiles have been identified in spicular sinters within high-temperature regimes (Handley et al., 2005, 2008; Sriaporn et al., 2020). It is possible that biofilms of extremophiles could have lived on exposed silica sinter surfaces in the high-altitude, arid conditions of El Tatio, such as halophiles or endoliths (Wierzchos et al., 2006). However, if unsheathed organisms were present on subaerial digitate surfaces, the relatively rapid, efficient degradation of such communities during or directly after silica entombment increases the difficulty in linking their existence to the digitate formation. Known pathways for cellular material degradation applicable to the El Tatio surface environment involve combined physical erosion, chemical/UV oxidation (Hartnett et al., 1998; Ward & Cory, 2016) and biological enzyme digestion (Kirchman, 2011). Remnants of unsheathed extremophile communities would thus have been relatively poorly preserved in the rapidly precipitating silica sinters.

Our detailed study of digitate sinter interiors did not reveal any fabrics or moulds indicating initially silicified microbial networks in these zones. LSM analysis also did not show any indication of remnant

cells, or remnant EPS in the subaerial surfaces (Figures 8–9, Figures S13, S14). There are, however, many voids in the sinter structure that could be interpreted as fenestrae which were created when initial biofilms degraded (Figures 4c,d, 5d–f, 6, Figure S11). Alternatively, though, these voids could represent space left out from dissolved salt crystals (Figures S9c, S17), or represent the general porosity of the sinter that was created during rapid silica precipitation. Apart from these voids, there are no indications for any trace of microbial activity.

5.3 | Biologic vs. abiotic factors in digitate sinter morphogenesis at El Tatio

Although we did not find evidence for microbial biofilms despite our high-resolution analyses, it is possible that such films were initially covering the sinter tips but their remnants were either degraded or not recognized. In that case, in order to template silica precipitation and dominate tilted digitate morphogenesis, these biofilms should have grown rapidly and preferentially on the wind-exposed parts of the sinters. However, there is no known ecologic advantage for biofilms growing in high wind fronts (Chénard & Lauro, 2017). Alternatively, if sticky biofilms were growing uniformly on all sides of the digitate surfaces, silica and sand grains could have adhered preferentially to the windward surfaces. This possibility cannot be ruled out; however, it is definitely not a requirement, since moist surfaces themselves can act as adhesion agents due to water tension. Saltating sand grains can stick onto capillary-moistened sediments (Kocurek & Fielder, 1982; Olsen et al., 1989), and several growth structures are known to result from such a process, including adhesion ripples, adhesion warts and asymmetric adhesion warts (Figure S16; Davies et al., 2016). These structures can indeed closely resemble microbially mediated sediments (Davies et al., 2016; Wilmeth et al., 2014). Therefore, taking into account the clear presence of silica-encrusted sand layers and the lack of observed biofilms or microbial mats that could have contributed to the primary layering, we suggest that digitate sinter formation at El Tatio appears to be dominated by sand saltation and wind-driven silica precipitation, while the effect of microbial templating was less pronounced or possibly even absent.

5.4 | Model for subaerial growth of tilted digitate sinters at El Tatio

In order for silica to precipitate onto subaerial surfaces, silica-enriched fluids need to be supplied by splashing, steam drift, wave action, water level fluctuations, wicking or capillary forces (Braunstein & Lowe, 2001; Handley et al., 2005; Lowe & Braunstein, 2003; Mountain et al., 2003; Schintie et al., 2007; Tobler et al., 2008). The presence of subaerial digitate structures at various distances from hot springs and geysers, but always directly adjacent to a water source (Figure 1, Figures S5–S8), excludes splashing or steam drifting as possible sources. Also, digitate structures are commonly found to be >5 mm above the maximum wave height during the day

(Figure S7, Table S1), excluding wave action as a viable process for silica supply. Rather, these observations suggest that silica-saturated fluids are delivered to the tops of digitate structures primarily by capillary forces, a process commonly observed in siliceous sinter fields (Braunstein & Lowe, 2001; Kocurek & Fielder, 1982; Olsen et al., 1989; Renaut et al., 1998). Seasonal or longer term water-level fluctuations and stream drifts (Schintie et al., 2007) could be additional processes that cause wet-dry cycles of the sinter. The efficiency of silica precipitation due to capillary forces critically depends on two main factors: (1) the relative duration and efficiency of the drying cycle and (2) the permeability and wetting ability of the previously deposited material (Caupin et al., 2008; Gruener et al., 2009). El Tatio's extreme dryness and the presence of high amounts of dissolved salts in fluids together seem to promote capillary transport through porous sinter structures (high porosity sinter following salt dissolution) (see Supplementary Time Lapse Video of capillary action experiment), while the action of wind brings additional detrital material for subaerial deposition (Figure 3).

Based on all environmental observations for wind, temperature, humidity fluctuations, field observations of the spatial distribution, orientation and height of digitate sinters, as well as their laminated interiors, and indications for capillary force as a main mechanism for silica supply, we here propose a model for the microenvironmentally driven formation process of subaerial components of tilted digitate sinters in the low- to mid-temperature regimes of the El Tatio geothermal field (Figure 10). As temperature and wind velocity decrease during the night, condensation allows surface rewetting, and silica-enriched fluids are given time to equilibrate within the sinter structure by molecular diffusion. In the morning when the wind is increasing it carries sand grains that occasionally attach to the wet silica sinter surfaces. As the day progresses and temperature and wind speed reach a maximum, evaporation drives capillary rise of salty and silica-rich spring fluids through the porous sinter structure, until the rate of capillary delivery cannot keep up with evaporation rates. At this point capillary fluid rise would cease, and occasional sand grains are glued in place as silica and salt precipitate. During a storm event, more sand grains are likely mobilized and attached than under normal conditions, generating a porous sand layer on the digitate surface. It is entirely possible that biofilms of extremophile micro-organisms are also initially colonizing the surfaces of these digitate sinters, and that they cause templating of silica. However, as was discussed in Sections 5.1 and 5.3, the universal windward orientation of the digitate sinters indicates that microenvironmental effects are the dominant factor for digitate morphogenesis.

Further observations and field-based precipitation experiments are required to quantify digitate growth rates, but silica-salt layers appear to be added diurnally while sand is predominantly added during storm events. The universal height of digitate structures throughout the basin suggests that the total stacking height of layers is restricted by an interplay between capillary force, gravity, wind-and-heat-driven evaporation, as well as the diffusion-driven, time-dependent equilibration of salty, silica-rich spring water with condensed fresh water.

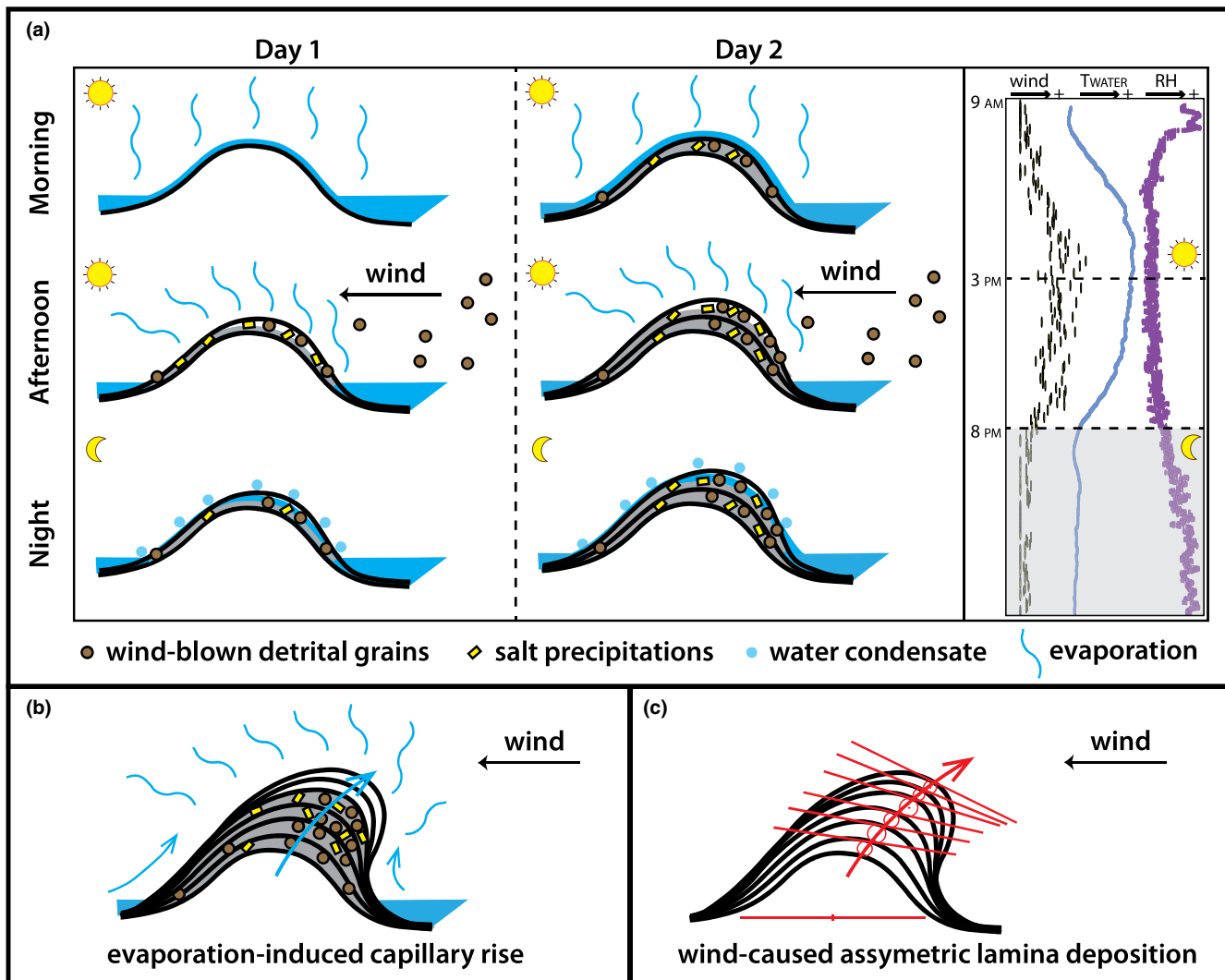


FIGURE 10 Proposed model for digitate structure formation in the El Tatio geothermal field. (a) The formation process of digitate laminae is demonstrated for two consecutive days. Day 1 Morning: water temperature rises after sunrise. Subaerial surfaces are wet due to condensation from the previous night. Evaporation increases with increasing temperature. Wind picks up while the local humid air is rapidly displaced by dry regional air, driving higher rates of evaporation. Afternoon: Wind reaches daily maximum, transporting and depositing detrital grains while the relative humidity of air reaches daily minimum and water/air temperature is at daily maximum. These three factors combine to drive the maximum rate of evaporation. Subaerial surfaces of digitate structures reach near-dryness, first precipitating out silica, binding and cementing deposited grains and then precipitating out salts. Night: wind reduces after sunset. Water temperature decreases while the relative humidity of air accumulates over the night. Water vapour condensation occurs on subaerial surfaces while salt and silica partially dissolve. Salty and silica-rich spring fluids equilibrate throughout the sinter structure by molecular diffusion. Day 2: The entire process repeats itself, forming another lamina. The patterns of wind, water temperature and air relative humidity were replotted against time from Figure 2 and are displayed on the right of the schematic. (b) The mechanism for the subaerial deposition of silica is the capillary rise of fluids due to surface tension. Fluids enriched in silica, sodium and chloride are therefore transported through a porous medium driven by surface evaporation. At night, condensation of water vapour on surfaces allows re-equilibration of silica and salts through the digitate structure. (c) Combined environmental scenarios driven by wind-induced evaporation and wind deposition of detrital materials explain the structural asymmetry of the digitate structures forming at El Tatio

5.5 | Implications for Geobiology and Astrobiology

Because subaerial digitate sinter morphogenesis at El Tatio appears to be primarily governed by wind-driven evaporation and deposition, we suggest that silica-enriched geothermal sources in any other arid, wind-dominated environment can form similar subaerial, tilted digitate sinter structures, without the requirement of dominant microbial surfaces for templating silica precipitation. This is relevant

for the interpretation of purported digitate sinters that have been recognized on Mars. Martian silica deposits adjacent to the Home Plate Formation in the Columbia Hills of Gusev Crater have been observed by NASA's Spirit Rover and interpreted in some studies as sinter deposits preserving ancient hot spring environments (Ruff & Farmer, 2016; Ruff et al., 2011; Squyres et al., 2008). The Columbia Hills deposits contain distinct digitate morphologies that closely resemble the subaerial digitate silica sinters at El Tatio (Ruff & Farmer,

2016). The environmental conditions at El Tatio are close to those of ancient Mars (Ruff & Farmer, 2016; Vago et al., 2017). It was stressed by Ruff and Farmer (2016), that it is unclear if the digitate structures on Mars are internally laminated or containing organics, thus these structures were classified as 'potential biosignatures', pending further investigation.

Based on our observations presented here for the digitate sinters of El Tatio, it is possible that Gusev crater sinters were produced in a cycle of evaporation and precipitation driven by changes in temperature, humidity and wind velocity in the presence of liquid water at the surface. The Martian digitate sinters therefore may not require a biologic component for their morphogenesis. As abiogenic structures, digitate sinters can still provide useful environmental proxies, such as evidence for subaerial exposure. For example, our model predicts that careful recording of digitate orientations on the surface of Mars can potentially be used as a palaeo-wind indicator.

6 | CONCLUSIONS

In conclusion, digitate silica sinters in the El Tatio geothermal field appear to form primarily through cyclic processes of evaporation and aeolian deposition, while templating effects by microbial surfaces may have had only minor or no effects on the resulting morphology. This means that digitate morphology alone is an insufficient proxy for biogenicity in deep time and astrobiology. However, these structures still remain sites of intense interest for studies of ancient life on Earth and Mars. It has been clearly shown in this study and previous work that digitate sinter structures require the presence of water for formation and can host microbial life, even if life did not actively produce them, acting as a shield for strong UV-radiation and other hostile conditions. In general, micro-organisms are known to pervasively colonize silica sinters, and to be very well preserved by silica encrustation, making these rocks clear targets for the search for direct remnant fossils, moulds and fabrics created by life.

ACKNOWLEDGEMENTS

This project has received funding from the European Research Coucil (ERC) under the European Union's Horizon 2020 Research and Innovation Programme (grant agreement n°646894) to M.A.V.Z. C.M-S. acknowledges support from CEGA-University of Chile, Conicyt. All fieldwork in the El Tatio Geothermal Field, Chile, was performed with the permission of the Amayras Communities of Caspana and Toconce. We acknowledge the analytical platform PARI at IPGP and Stefan Borenstazjn for assistance with SEM imaging. This study contributes to the IdEx Université de Paris ANR-18-IDEX-0001. This is IPGP contribution nr.4237.

AUTHOR CONTRIBUTIONS

J.G. undertook fieldwork, field meteorological observations, acquisition of digitate sinter samples and subsequent optical microscopy imaging, SEM analysis, and interpretation of the results. C.M-S. provided support for fieldwork, obtained general meteorological data,

and interpreted the results. D.T.W. assisted with fieldwork and interpreted the internal layering and fabrics of digitate sinters. K.D.M. interpreted the microbiological field observations, microbial distribution in silica sinters and performed XRF-scanning. M.H. assisted with XRF-scanning and provided interpretations. J.R.S. assisted with detailed drone imaging of field areas and image construction and interpretation. G.A. performed fluorescence imaging analysis on the digitate sinter samples and provided interpretations. M.A.V.Z. undertook fieldwork and interpretation of the results. J.G. and M.A.V.Z. wrote the paper and all authors read and contributed to the work.

DATA AVAILABILITY STATEMENT

The data that support the findings of this study are openly available in figshare at <https://doi.org/10.6084/m9.figshare.12957797.v1>.

ORCID

Jian Gong  <https://orcid.org/0000-0001-7214-1628>

Dylan T. Wilmeth  <https://orcid.org/0000-0002-6299-6267>

Gernot Arp  <https://orcid.org/0000-0002-0968-7916>

Mark A. van Zuilen  <https://orcid.org/0000-0001-6723-6366>

REFERENCES

- Bartley, J. K. (1996). Actualistic taphonomy of cyanobacteria: Implications for the precambrian fossil record. *Palaios*, 11, 571–586. <https://doi.org/10.2307/3515192>
- Belton, D. J., Deschaume, O., & Perry, C. C. (2012). An overview of the fundamentals of the chemistry of silica with relevance to biosilicification and technological advances. *FEBS Journal*, 279, 1710–1720. <https://doi.org/10.1111/j.1742-4658.2012.08531.x>
- Benning, L. G., Phoenix, V. R., Yee, N., & Konhauser, K. O. (2004). The dynamics of cyanobacterial silicification: An infrared microspectroscopic investigation. *Geochimica et Cosmochimica Acta*, 68, 743–757. [https://doi.org/10.1016/S0016-7037\(03\)00488-5](https://doi.org/10.1016/S0016-7037(03)00488-5)
- Bosak, T., Bush, J. W. M., Flynn, M. R., Liang, B., Ono, S., Petroff, A. P., & Sim, M. S. (2010). Formation and stability of oxygen-rich bubbles that shape photosynthetic mats. *Geobiology*, 8, 45–55. <https://doi.org/10.1111/j.1472-4669.2009.00227.x>
- Bosak, T., Knoll, A. H., & Petroff, A. P. (2013). The meaning of stromatolites. *Annual Review of Earth and Planetary Sciences*, 41, 21–44. <https://doi.org/10.1146/annurev-earth-042711-105327>
- Bosak, T., Liang, B., Sim, M. S., & Petroff, A. P. (2009). Morphological record of oxygenic photosynthesis in conical stromatolites. *Proceedings of the National Academy of Sciences United States of America*, 106, 10939–10943. <https://doi.org/10.1073/pnas.0900885106>
- Bosak, T., Liang, B., Wu, T.-D., Templer, S. P., Evans, A., Vali, H., Guerquin-Kern, J.-L., Klepac-Ceraj, V., Sim, M. S., & Mui, J. (2012). Cyanobacterial diversity and activity in modern conical microbiolites. *Geobiology*, 10, 384–401. <https://doi.org/10.1111/j.1472-4669.2012.00334.x>
- Braunstein, D., & Lowe, D. R. (2001). Relationship between spring and Geyser activity and the deposition and morphology of high temperature (> 73°C) Siliceous Sinter, Yellowstone National Park, Wyoming, U.S.A. *Journal of Sedimentary Research*, 71, 747–763.
- Cabrol, N. A., Feister, U., Häder, D.-P., Piazzena, H., Grin, E. A., & Klein, A. (2014). Record solar UV irradiance in the tropical Andes. *Frontiers in Environmental Science*, 2, 19. <https://doi.org/10.3389/fenvs.2014.00019>
- Cady, S. L., & Farmer, J. D. (1996). Fossilization processes in siliceous thermal springs: Trends in preservation along thermal gradients. *Ciba Foundation Symposium*, 202, 150–170, discussion 170–173.

- Cady, S. L., Farmer, J. D., Grotzinger, J. P., Schopf, J. W., & Steele, A. (2003). Morphological biosignatures and the search for life on mars. *Astrobiology*, 3, 351–368. <https://doi.org/10.1089/153110703769016442>
- Castenholz, R. W., Wilmotte, A., Herdman, M., Rippka, R., Waterbury, J. B., Iteman, I., & Hoffmann, L. (2001) Phylum BX. Cyanobacteria. In: D. R. Boone, R. W. Castenholz, & G. M. Garrity, *Bergey's Manual® of systematic bacteriology: Volume One : The archaea and the deeply branching and phototrophic bacteria*, (pp. 473–599). Springer.
- Caupin, F., Cole, M. W., Balibar, S., & Treiner, J. (2008). Absolute limit for the capillary rise of a fluid. *EPL (Europhysics Letters)*, 82, 56004. <https://doi.org/10.1209/0295-5075/82/56004>
- Chan, S. H. (1989). A review on solubility and polymerization of silica. *Geothermics*, 18, 49–56. [https://doi.org/10.1016/0375-6505\(89\)90009-6](https://doi.org/10.1016/0375-6505(89)90009-6)
- Chénard, C., & Lauro, F. M. (Eds.) (2017). *Microbial ecology of extreme environments*, 1st ed: Springer.
- Cortecci, G., Boschetti, T., Mussi, M., Lameli, C. H., Mucchino, C., & Barbieri, M. (2005). New chemical and original isotopic data on waters from El Tatio geothermal field, Northern Chile. *Geochemical Journal*, 39, 547–571. <https://doi.org/10.2343/geochemj.39.547>
- Davies, N. S., Liu, A. G., Gibling, M. R., & Miller, R. F. (2016). Resolving MISS conceptions and misconceptions: A geological approach to sedimentary surface textures generated by microbial and abiotic processes. *Earth-Science Reviews*, 154, 210–246. <https://doi.org/10.1016/j.earscirev.2016.01.005>
- Fernandez-Turiel, J. L., Garcia-Valles, M., Gimeno-Torrente, D., Saavedra-Alonso, J., & Martinez-Manent, S. (2005). The hot spring and Geyser sinters of El Tatio, Northern Chile. *Sedimentary Geology*, 180, 125–147. <https://doi.org/10.1016/j.sedgeo.2005.07.005>
- Fournier, R. O., & Rowe, J. J. (1966). Estimation of underground temperatures from the silica content of water from hot springs and wet-steam wells. *American Journal of Science*, 264, 685–697. <https://doi.org/10.2475/ajs.264.9.685>
- Gong, J. (2021). Morphogenesis of digitate structures in hot spring silica sinters of the El Tatio geothermal field. Chile. figshare. Figure, <https://doi.org/10.6084/m9.figshare.12957797.v1>
- Gong, J., Myers, K. D., Munoz-Saez, C., Homann, M., Rouillard, J., Wirth, R., Schreiber, A., & van Zuilen, M. A. (2020). Formation and preservation of microbial palisade fabric in silica deposits from El Tatio, Chile. *Astrobiology*, 20, 500–524. <https://doi.org/10.1089/ast.2019.2025>
- Gruener, S., Hofmann, T., Wallacher, D., Kityk, A. V., & Huber, P. (2009). Capillary rise of water in hydrophilic nanopores. *Physical Review E*, 79, e067301. <https://doi.org/10.1103/PhysRevE.79.067301>
- Guido, D. M., Campbell, K. A., Foucher, F., & Westall, F. (2019). Life is everywhere in sinters: Examples from Jurassic hot-spring environments of Argentine Patagonia. *Geological Magazine*, 156, 1631–1638. <https://doi.org/10.1017/S0016756819000815>
- Guidry, S. A., & Chafetz, H. S. (2002). Factors governing subaqueous siliceous sinter precipitation in hot springs: Examples from Yellowstone National Park, USA. *Sedimentology*, 49, 1253–1267. <https://doi.org/10.1046/j.1365-3091.2002.00494.x>
- Guidry, S. A., & Chafetz, H. S. (2003). Anatomy of siliceous hot springs: Examples from Yellowstone National Park, Wyoming, USA. *Sedimentary Geology*, 157, 71–106. [https://doi.org/10.1016/S0037-0738\(02\)00195-1](https://doi.org/10.1016/S0037-0738(02)00195-1)
- Handley, K. M., Campbell, K. A., Mountain, B. W., & Browne, P. R. L. (2005). Abiotic-biotic controls on the origin and development of spicular sinter. In situ growth experiments, Champagne Pool, Waiotapu, New Zealand. *Geobiology*, 3, 93–114. <https://doi.org/10.1111/j.1472-4669.2005.00046.x>
- Handley, K. M., Turner, S. J., Campbell, K. A., & Mountain, B. W. (2008). Silicifying biofilm exopolymers on a hot-spring microstromatolite: Templating nanometer-thick laminae. *Astrobiology*, 8, 747–770. <https://doi.org/10.1089/ast.2007.0172>
- Harrison, J. P., Gheeraert, N., Tsigelnitskiy, D., & Cockell, C. S. (2013). The limits for life under multiple extremes. *Trends in Microbiology*, 21, 204–212. <https://doi.org/10.1016/j.tim.2013.01.006>
- Hartnett, H. E., Keil, R. G., Hedges, J. I., & Devol, A. H. (1998). Influence of oxygen exposure time on organic carbon preservation in continental margin sediments. *Nature*, 391, 572–575. <https://doi.org/10.1038/35351>
- Hurwitz, S., & Manga, M. (2017). The fascinating and complex dynamics of geyser eruptions. *Annual Review of Earth and Planetary Sciences*, 45, 31–59. <https://doi.org/10.1146/annurev-earth-063016-015605>
- Iler, R. K. (1979). *The chemistry of silica: Solubility, polymerization, colloid and surface properties and biochemistry of silica*: Wiley-Interscience.
- Jones, B., Konhauser, K. O., Renaut, R. W., & Wheeler, R. S. (2004). Microbial silicification in iodine pool, Waimangu geothermal area, North Island, New Zealand: Implications for recognition and identification of ancient silicified microbes. *Journal of the Geological Society*, 161, 983–993. <https://doi.org/10.1144/0016-764903-172>
- Jones, B., & Renaut, R. W. (1997). Formation of silica oncoids around geysers and hot springs at El Tatio, Northern Chile. *Sedimentology*, 44, 287–304. <https://doi.org/10.1111/j.1365-3091.1997.tb01525.x>
- Jones, B., & Renaut, R. W. (2003). Petrography and genesis of spicular and columnar geyserite from the Whakarewarewa and Orakeikorako Geothermal Areas, North Island, New Zealand. *Canadian Journal of Earth Sciences*, 40, 1585–1610. <https://doi.org/10.1139/e03-062>
- Jones, B., Renaut, R. W., & Rosen, M. R. (1997). Biogenicity of silica precipitation around geysers and hot-spring vents, North Island, New Zealand. *Journal of Sedimentary Research*, 67, 88–104
- Kirchman, D. L. (2011). *Degradation of organic material*: Oxford University Press.
- Kocurek, G., & Fielder, G. (1982). Adhesion structures. *Journal of Sedimentary Research*, 52, 1229–1241.
- Kok, J. F., Parteli, E. J. R., Michaels, T. I., & Karam, D. B. (2012). The physics of wind-blown sand and dust. *Reports on Progress in Physics*, 75, 106901. <https://doi.org/10.1088/0034-4885/75/10/106901>
- Konhauser, K. O., Jones, B., Phoenix, V. R., Ferris, G., & Renaut, R. W. (2004). The microbial role in hot spring silicification. *AMBIO: A Journal of the Human Environment*, 33, 552–558. <https://doi.org/10.1579/0044-7447-33.8.552>
- Langsrud, S., & Sundheim, G. (1996). Flow cytometry for rapid assessment of viability after exposure to a quaternary ammonium compound. *Journal of Applied Bacteriology*, 81, 411–418. <https://doi.org/10.1111/j.1365-2672.1996.tb03527.x>
- Lowe, D. R., & Braunstein, D. (2003). Microstructure of high-temperature (>73 °C) siliceous sinter deposited around hot springs and geysers, Yellowstone National Park: The role of Biological and Abiological Processes in Sedimentation. *Canadian Journal of Earth Sciences*, 40, 1611–1642.
- Lucchi, F., Tranne, C. A., Rossi, P. L., De Astis, G., & Pini, G. A. (2009). Volcanic and tectonic history of El Tatio area (Central Andes, Northern Chile): Explanatory notes to the 1:50000 scale geological map. *GeoActa*, 2, 1–29.
- Lynne, B. Y. (2012). Mapping vent to distal-apron hot spring Paleo-flow pathways using siliceous sinter architecture. *Geothermics*, 43, 3–24. <https://doi.org/10.1016/j.geothermics.2012.01.004>
- Mlewska, E. C., Pisapia, C., Gomez, F., Lecourt, L., Soto Rueda, E., Benzerara, K., Ménez, B., Borensztajn, S., Jamme, F., Réfrégiers, M., & Gérard, E. (2018). Characterization of pustular mats and related Rivularia-Rich laminations in oncoids from the Laguna Negra Lake (Argentina). *Frontiers in Microbiology*, 9, 996.
- Mountain, B. W., Benning, L. G., & Boerema, J. A. (2003). Experimental studies on New Zealand hot spring sinters: Rates of growth and textural development. *Canadian Journal of Earth Sciences*, 40, 1643–1667. <https://doi.org/10.1139/e03-068>
- Munoz-Saez, C., Manga, M., & Hurwitz, S. (2018). Hydrothermal discharge from the El Tatio basin, Atacama, Chile. *Journal of Volcanology and*

- Geothermal Research*, 361, 25–35. <https://doi.org/10.1016/j.jvolgfores.2018.07.007>
- Munoz-Saez, C., Manga, M., Hurwitz, S., Slagter, S., Churchill, D. M., Reich, M., Damby, D., & Morata, D. (2020). Radiocarbon dating of silica sinter and postglacial hydrothermal activity in the El Tatio Geyser Field. *Geophysical Research Letters*, 47, e2020GL087908. <https://doi.org/10.1029/2020GL087908>
- Nicolau, C., Reich, M., & Lynne, B. (2014). Physico-chemical and environmental controls on siliceous sinter formation at the high-altitude El Tatio Geothermal Field, Chile. *Journal of Volcanology and Geothermal Research*, 282, 60–76. <https://doi.org/10.1016/j.jvolgfores.2014.06.012>
- Olsen, H., Due, P. H., & Clemmensen, L. B. (1989). Morphology and genesis of asymmetric adhesion warts—A new adhesion surface structure. *Sedimentary Geology*, 61, 277–285. [https://doi.org/10.1016/0037-0738\(89\)90062-6](https://doi.org/10.1016/0037-0738(89)90062-6)
- Pepe-Ranney, C., Berelson, W. M., Corsetti, F. A., Treants, M., & Spear, J. R. (2012). Cyanobacterial construction of hot spring siliceous stromatolites in Yellowstone National Park. *Environmental Microbiology*, 14, 1182–1197. <https://doi.org/10.1111/j.1462-2920.2012.02698.x>
- Petroff, A. P., Beukes, N. J., Rothman, D. H., & Bosak, T. (2013). Biofilm growth and fossil form. *Physical Review X*, 3, e041012. <https://doi.org/10.1103/PhysRevX.3.041012>
- Petroff, A. P., Sim, M. S., Maslov, A., Krupenin, M., Rothman, D. H., & Bosak, T. (2010). Biophysical basis for the geometry of conical stromatolites. *Proceedings of the National Academy of Sciences United States of America*, 107, 9956–9961. <https://doi.org/10.1073/pnas.1001973107>
- Phoenix, V. R., Bennett, P. C., Engel, A. S., Tyler, S. W., & Ferris, F. G. (2006). Chilean high-altitude hot-spring sinters: A model system for UV screening mechanisms by early precambrian cyanobacteria. *Geobiology*, 4, 15–28. <https://doi.org/10.1111/j.1472-4669.2006.00063.x>
- Renaut, R. W., Jones, B., & Rosen, M. R. (1996). Primary silica oncoids from Orakeikorako hot springs, North Island, New Zealand. *Palaios*, 11, 446–458. <https://doi.org/10.2307/3515212>
- Renaut, R. W., Jones, B., & Tiercelin, J.-J. (1998). Rapid in situ silicification of microbes at Loburu hot springs, Lake Bogoria, Kenya rift valley. *Sedimentology*, 45, 1083–1103.
- Rice, M. A., Willets, B. B., & McEWAN, I. K. (1995). An experimental study of multiple grain-size ejecta produced by collisions of saltating grains with a flat bed. *Sedimentology*, 42, 695–706. <https://doi.org/10.1111/j.1365-3091.1995.tb00401.x>
- Ruff, S. W., Campbell, K. A., Van Kranendonk, M. J., Rice, M. S., & Farmer, J. D. (2020). The case for ancient hot springs in Gusev Crater, Mars. *Astrobiology*, 20(4), 475–499
- Ruff, S. W., & Farmer, J. D. (2016). Silica deposits on mars with features resembling hot spring biosignatures at El Tatio in Chile. *Nature Communications*, 7, 13554. <https://doi.org/10.1038/ncomms13554>
- Ruff, S. W., Farmer, J. D., Calvin, W. M., Herkenhoff, K. E., Johnson, J. R., Morris, R. V., Rice, M. S., Arvidson, R. E., Bell, J. F., Christensen, P. R., & Squyres, S. W. (2011). Characteristics, distribution, origin, and significance of opaline silica observed by the spirit rover in Gusev Crater, Mars. *Journal of Geophysical Research: Planets*, 116, E00F23. <https://doi.org/10.1029/2010JE003767>
- Sambrook, J. F., & Russel, D. W. (2001). *Molecular cloning: A laboratory manual*, 3rd ed: Cold Spring Harbor Laboratory Press.
- Schintie, R., Campbell, K., & Browne, P. (2007). Microfacies of stromatolitic sinter from acid-sulphate-chloride springs at Parakiri Stream, Rotokawa geothermal field, New Zealand. *Palaeontologia Electronica*, 10(4A), 33.
- Shepard, R. N., & Sumner, D. Y. (2010). Undirected motility of filamentous cyanobacteria produces reticulate mats. *Geobiology*, 8, 179–190. <https://doi.org/10.1111/j.1472-4669.2010.00235.x>
- Slagter, S., Reich, M., Munoz-Saez, C., Southon, J., Morata, D., Barra, F., Gong, J., & Skok, J. R. (2019). Environmental controls on silica sinter formation revealed by radiocarbon dating. *Geology*, 47, 330–334. <https://doi.org/10.1130/G45859.1>
- Squyres, S. W., Arvidson, R. E., Ruff, S., Gellert, R., Morris, R. V., Ming, D. W., Crumpler, L., Farmer, J. D., Marais, D. J. D., Yen, A., McLennan, S. M., Calvin, W., Bell, J. F., Clark, B. C., Wang, A., McCoy, T. J., Schmidt, M. E., & de Souza, P. A. (2008). Detection of silica-rich deposits on mars. *Science*, 320, 1063–1067. <https://doi.org/10.1126/science.1155429>
- Sriaporn, C., Campbell, K. A., Millan, M., Ruff, S. W., Kranendonk, M. J. V., & Handley, K. M. (2020). Stromatolitic digitate sinters form under wide-ranging physicochemical conditions with diverse hot spring microbial communities. *Geobiology*, 18, 619–640.
- Tassi, F., Martinez, C., Vaselli, O., Capaccioni, B., & Viramonte, J. (2005). Light Hydrocarbons as redox and temperature indicators in the geo-thermal field of El Tatio (northern Chile). *Applied Geochemistry*, 20, 2049–2062. <https://doi.org/10.1016/j.apgeochem.2005.07.013>
- Tobler, D. J., Stefánsson, A., & Benning, L. G. (2008). In-situ grown silica sinters in icelandic geothermal areas. *Geobiology*, 6, 481–502.
- Vago, J. L., Westall, F., Coates, A. J., Jaumann, R., Koralev, O., Ciarletti, V., Mitrofanov, I., Josset, J. L., De Sanctis, M. C., Bibring, J. P., Rull, F., Goesmann, F., Steininger, H., Goetz, W., Brinckerhoff, W., Szopa, C., Raulin, F., Westall, F., ... Edwards, H. G. M. (2017). Habitability on early mars and the search for biosignatures with the ExoMars Rover. *Astrobiology*, 17, 471–510. <https://doi.org/10.1089/ast.2016.1533>
- Ward, C. P., Cory, R. M. (2016). Complete and Partial Photo-oxidation of Dissolved Organic Matter Draining Permafrost Soils. *Environmental Science & Technology*, 50, 3545–3553.
- Walter, M. R., Bauld, J., & Brock, T. D. (1972). Siliceous algal and bacterial stromatolites in hot spring and geyser effluents of Yellowstone National Park. *Science*, 178, 402–405. <https://doi.org/10.1126/science.178.4059.402>
- Walter, M. R., & Des Marais, D. J. (1993). Preservation of biological information in thermal spring deposits: Developing a strategy for the search for fossil life on mars. *Icarus*, 101, 129–143. <https://doi.org/10.1006/icar.1993.1011>
- Walter, M. R. (1976) Chapter 3.3 geyserites of Yellowstone National Park: An example of abiogenic "Stromatolites". In: M. R. Walter, *Developments in sedimentology, Stromatolites*, (pp. 87–112): Elsevier.
- Wierzchos, J., Ascaso, C., & McKay, C. P. (2006). Endolithic cyanobacteria in Halite Rocks from the hyperarid core of the Atacama Desert. *Astrobiology*, 6, 415–422. <https://doi.org/10.1089/ast.2006.6.415>
- Wilmeth, D. T., Dornbos, S. Q., Isbell, J. L., & Czaja, A. D. (2014). Putative domal microbial structures in fluvial siliciclastic facies of the Mesoproterozoic (1.09 Ga) Copper Harbor Conglomerate, Upper Peninsula of Michigan, USA. *Geobiology*, 12, 99–108.
- Wilmeth, D. T., Myers, K. D., Lalonde, S. V., Mänd, K., Konhauser, K. O., Grandin, P., van Zuilen, M. A. (in press, 2021). Evaporative silicification in floating microbial mats: patterns of oxygen production and preservation potential in silica-undersaturated streams, El Tatio, Chile. *Geobiology*.

SUPPORTING INFORMATION

Additional supporting information may be found in the online version of the article at the publisher's website.

How to cite this article: Gong, J., Munoz-Saez, C., Wilmeth, D. T., Myers, K. D., Homann, M., Arvidson, R. E., Skok, J. R., & van Zuilen, M. A. (2022). Morphogenesis of digitate structures in hot spring silica sinters of the El Tatio geothermal field, Chile. *Geobiology*, 20, 137–155. <https://doi.org/10.1111/gbi.12471>